

Signature of reentrant localization in collisional inhomogeneous spin-orbit coupled condensates

Swarup K. Sarkar,¹ Rajamanickam Ravisankar,^{2,3} Tapan Mishra,^{4,5} Paulsamy Muruganandam,⁶ and Pankaj Mishra¹

¹*Department of Physics, Indian Institute of Technology Guwahati, Guwahati 781039, Assam, India*

²*Department of Physics, Zhejiang Normal University, Jinhua 321004, PR China*

³*Zhejiang Institute of Photoelectronics & Zhejiang Institute for Advanced Light Source, Zhejiang Normal University, Jinhua, Zhejiang 321004, China*

⁴*School of Physical Sciences, National Institute of Science Education and Research, Jatni 752050, India*

⁵*Homi Bhabha National Institute, Training School Complex, Anushaktinagar, Mumbai 400094, India*

⁶*Department of Physics, Bharathidasan University, Tiruchirappalli 620024, Tamilnadu, India*

(Dated: March 12, 2024)

We study the localization transition in a spin-orbit (SO) coupled binary Bose-Einstein condensates (BECs) with collisional inhomogeneous interaction trapped in a one-dimensional quasiperiodic potential. Our numerical analysis shows that the competition between the quasiperiodic disorder and inhomogeneous interaction leads to a reentrant localization transition as the interaction strength is tuned from attractive to repulsive in nature. Further, we analyse the combined effect of the SO and Rabi coupling strengths on the localization transition for different interaction strengths and obtain signatures of reentrant localization transition as function of SO coupling in the regime of weak interactions. We complement our numerical observation with the analytical model using the variational approach. At the end we show how the reentrant localization is manifested in the quench dynamics of the condensate. Our study provides an indirect approach to achieve localization transition without tuning the quasiperiodic potential strength, rather by tuning the inhomogeneous interaction.

I. INTRODUCTION

After the path breaking prediction of exponential localization of electronic wavefunction in random media by Anderson, the study of localization transition has attracted a great deal of attention in condensed matter [1–5]. Recent developments in the experimental front, such as localization transitions have been observed in various artificial systems such as electromagnetic waves [6–10], microwaves [11–14], acoustic waves [15], quantum matter waves [16, 17], and in the non-interacting [18] and interacting Bose-Einstein condensates (BECs) [19].

Among the various platforms, enormous progress has been made in studying localization transition in systems of BECs in random and quasiperiodic lattices due to the flexibility in controlling the geometry and interaction. In this context, more complex systems have been considered recently, such as the binary BECs [20–22], spin-orbit (SO) coupled spinor BECs, etc. [23–28]. Theoretically, it has been demonstrated that the SO coupling influences the appearance of localization, whereas the Rabi coupling slightly promotes the delocalization [29]. Akin to SO coupling, interactions among atoms play a vital role in dictating the localization-delocalization phenomena in the condensate. For instance, several numerical studies show that the increase of repulsive interaction induces the localization to delocalization transitions for the condensate trapped in the disordered potential [30–35]. Subsequent studies have reported the symmetry breaking of a localized binary condensate in the presence of inter-species and intra-species atomic interactions [34, 36]. Santos and Cardoso demonstrated that even with only one component subjected to the quasiperiodic potential, the inter-

species interaction induces the localization in the other component [27].

On the other hand, localization transition has been achieved by spatial variation of atomic scattering length leading to *collisionally inhomogeneous* environment [37, 38]. A great deal of effort has been made in exploring areas like adiabatic compression of matter waves [39–42], dynamical trapping of matter wave solutions [43], soliton oscillations [44, 45], BECs in nonlinear optical lattices [46], and localization in the scalar [35, 47] or binary BECs [48]. The investigations on localization in the presence of *collisionally inhomogeneous* environment reveal the effect of spatially dependent interaction towards localization as a result of the genesis of an effective potential whereas, without the inhomogeneity, the atomic interaction leads to delocalization of the condensate [35, 47, 48].

Apart from the standard delocalization-localization transition, a new class of localization transition known as the reentrant localization transition in quasiperiodic lattices has attracted a great deal of attention in recent years. While in the conventional localization transition, the states after the localization transition remain localized with an increase in the disorder in the system, in the case of reentrant localization, the localized system delocalizes again before getting localized for the second time as a function of the quasiperiodic potential strength [49–51]. Such intriguing reentrant localization has been studied extensively in recent years [52], including in non-Hermitian lattices [53], leading to their experimental observations [54–57]. In the continuum systems, however, this kind of reentrant localization has not been analyzed with the same rigour as those in the strongly

correlated system. Although a recent study has revealed the reentrant of localization upon variation of SO coupling in a *non-interacting* condensate trapped in a disordered quasiperiodic potential [25], a complete understanding of the reentrant localization for weakly *interacting* BECs is lacking.

In this work, we present an extensive numerical study that explores the impact of inhomogeneous interactions in the localization of SO coupled BECs subjected to a bichromatic quasiperiodic optical lattice potential. We consider the spatial dependent interactions induced by the external optical fields to have the same form as the bichromatic potential with the parameters depending on the intensity of the lasers [58, 59]. This setting leads to the localization of the condensate with the variation of interaction strength. However, by implementing an additional phase shift $\pi/2$ between the inhomogeneous interaction and trapping potential, we obtain the signature of reentrant localization transition, where we find an intermediate delocalized phase sandwiched between two localized phases with the variation of the strength of the inhomogeneity of the nonlinearity. Furthermore, we complement this reentrant behaviour in the localization through the Gaussian variational approach. At last, we obtain the signatures of such localization properties from the dynamical behaviour of the condensate.

The paper is structured as follows: Section II introduces a mean-field theoretical model to examine SO coupled BECs in a quasiperiodic optical lattice potential with spatially varying interactions. Section III A presents the numerical results, starting from condensate densities depending on inhomogeneous interactions and various coupling parameters. Here, we characterize the localized and delocalized states using the form factor and condensate width. Section III B explores the role of inhomogeneous interactions in demonstrating the reentrant behaviour of condensate localization. A variational approach is also employed to understand the behaviour of the localization using the effective potential. Section III D investigates the dynamics of localized and delocalized condensates under velocity perturbations and trap quenching. Finally, Section IV provides a summary and conclusion. Appendices A and B provide detailed equations of motion and discussions on variational approaches and Lagrangian details, respectively, along with numerical and variational comparison and energy analysis.

II. GOVERNING DYNAMICAL MEAN-FIELD EQUATION AND SIMULATION DETAILS

We consider a pseudo spin-1/2 quasi-1D condensate with strong transverse confinement, modelled using the

coupled Gross-Pitaevskii equations (GPEs) as,

$$i\frac{\partial\psi_1}{\partial t} = \left[-\frac{1}{2}\frac{\partial^2}{\partial x^2} + (g_{11}|\psi_1|^2 + g_{12}|\psi_2|^2) + V(x) \right] \psi_1 - ik_L\frac{\partial\psi_1}{\partial x} + \Omega\psi_2, \quad (1a)$$

$$i\frac{\partial\psi_2}{\partial t} = \left[-\frac{1}{2}\frac{\partial^2}{\partial x^2} + (g_{22}|\psi_2|^2 + g_{21}|\psi_1|^2) + V(x) \right] \psi_2 + ik_L\frac{\partial\psi_2}{\partial x} + \Omega\psi_1, \quad (1b)$$

where ψ_1 and ψ_2 represent the wavefunctions for pseudo spin-up and spin-down components, respectively. Here, g_{11} and g_{22} are the intra-species nonlinearities for spin-up and spin-down components, and g_{12} represents the interspecies interaction strength. k_L is the SO coupling strength and Ω is the Rabi coupling strength. $V(x)$ represents the trapping potential. For our studies, we consider $g_{11} = g_{22} = g$. The wave functions follow the normalization condition as

$$\int_{-\infty}^{\infty} (|\psi_1|^2 + |\psi_2|^2) dx = 2. \quad (2)$$

To obtain the non-dimensionalized Eq. 1, we consider the transverse harmonic oscillator length $a_{\perp} = \sqrt{\hbar/(m\omega_{\perp})}$ as a characteristic length scale with ω_{\perp} as the transverse harmonic trapping frequency, ω_{\perp}^{-1} as the timescale and $\hbar\omega_{\perp}$ as the characteristic energy scale. The interaction parameters can be defined in terms of $g = 2Na_{11}/a_{\perp}$, and $g_{12} = 2Na_{12}/a_{\perp}$, where a_{11} and a_{12} represent the intra-component and inter-component scattering lengths, respectively. The SO coupling is re-scaled as $k_L \equiv k'_L a_{\perp}$ and Rabi coupling as $\Omega \equiv \Omega'/(2\omega_{\perp})$. The wavefunction is rescaled as $\psi_{1,2}(x, t) \equiv \psi'_{1,2}(x, t)\sqrt{a_{\perp}}$. Here variables with prime represent the dimensional quantities.

To analyze the characteristics and dynamics of the localization of the condensate, we consider a quasiperiodic trapping potential $V(x)$ of the form [25],

$$V(x) = -V_1 \cos(k_1 x) - V_2 \cos(k_2 x), \quad (3)$$

where V_1 and V_2 are the primary and secondary optical lattice amplitudes, respectively. For all calculations, we consider the primary and secondary lattice strengths as $V_1 = 1$ and $V_2 = 0.1$, respectively, with the angular wavenumber ratio as the golden ratio, i.e., $k_2/k_1 = (\sqrt{5} + 1)/2$. With this angular wave number, the wavelength of the laser beams will have the values as $\lambda_1 \approx 3.1415a_{\perp}$ and $\lambda_2 \approx 1.9416a_{\perp}$, respectively, where a_{\perp} denotes the characteristic length scale approximately equal to $1.17\mu\text{m}$. Note that in the experiment of Roati *et al.* [19], the ratio k_2/k_1 is 1.1971.

To make the parameters considered in numerical simulations experimentally feasible, we consider the two hyperfine states of ^{87}Rb atom as pseudo spin-up state

$|1\rangle \equiv |F=1, m_F=0\rangle$, and pseudo spin-down state $|2\rangle \equiv |F=1, m_F=-1\rangle$. Following the experiment of Lin *et al.* [23], we consider $N \sim 1.8 \times 10^5$ number of atoms in a harmonic trap strongly confined along the perpendicular direction with frequency $\omega_{\perp} \approx 2\pi \times 83.66$ Hz, and along the axial direction the trapping frequency is chosen to be $\omega_x \approx 2\pi \times 7.07$ Hz. In the experiment, the wavelength of the Raman lasers, $\lambda_L = 804.1$ nm and its geometry provide a tool for tuning the SO-coupling strength (k_L). The SO coupling strength k_L can be tuned within the range $k'_L = [0.1 - 4]a_{\perp}$ using a pair of Raman lasers. On the other hand, the intensity of the Raman lasers is attributed to the variation of Rabi coupling frequency Ω , where, in experiments, it can be adjusted within the interval $\Omega' = 2\pi \times [105.13 - 669.28]$ Hz, which is associated to the dimensionless Rabi-coupling frequency $\Omega = [0.1 - 4]$. Furthermore, by choosing the s-wave scattering length values between $a_{11} = a_{22} = [-0.0866a_0, 0.0866a_0]$ the intra-species interaction parameters can be adjusted between $g_{22} = g_{11} = [-1, 1]$. Similarly, for inter-species interaction parameters g_{12} , the scattering length a_{12} can be varied from $-0.0866a_0$ to $0.0866a_0$, where a_0 is the Bohr radius.

One of the main focuses of the present work is to show the role of inhomogeneity in the interaction, describing the localization and delocalization of the condensate. For that, here we provide a generalized expression for the spatial dependence of the atomic scattering length depending upon the intensity $I(x)$ and detuning parameter of the laser beam. In general, the spatial dependence of the scattering length can be expressed as [37, 38, 47, 58],

$$a(x) = a^0 + \frac{\alpha I(x)}{\gamma_s + \beta I(x)} \quad (4a)$$

$$a_{12}(x) = a_{12}^0 + \frac{\alpha I(x)}{\gamma_s + \beta I(x)} \quad (4b)$$

Here, a^0 and a_{12}^0 denote the intra- and interspecies s-wave scattering lengths when the optical fields are absent. α and β are the constants depending upon the laser detuning [38]. γ_s is the spontaneous decay rate between two atomic levels. In the experiment, the laser detuning is considered to be larger than the spontaneous decay rate that minimizes the decay of atomic state, which in turn helps to realize the optical Feshbach resonance. Here, $I(x)$ is the intensity of the laser beam generated due to the stimulated transition between two atomic states [60–62].

Theis *et al.* [38] experimentally demonstrated that the scattering length of ^{87}Rb condensate can be measured upon variation of laser detuning utilizing the optical Feshbach resonance technique. They estimated that the scattering length a is within the range $10a_0$ to $190a_0$, considering the background scattering length value of ^{87}Rb as $a^0 = 100a_0$ resulting in the variation of the scattering length in the range $-90a_0$ to $+90a_0$. One can tune the interaction from attractive to repulsive regions with the

above technique. The spatial dependence of the scattering length $a(x)$ can be achieved using the space dependence intensity, $I(x)$ of the laser beam. Without loss of generality, it is reasonable to consider the nonlinearity proportional to the optical lattice potential $V(x)$, as it is created using the laser field intensity [35, 48, 58]. In this work, we assume $a_{11}(x) = a_{22}(x) = a(x)$. With this consideration, $g_{11}(x)$, $g_{22}(x)$ and $g_{12}(x)$ can be written as,

$$g_{11}(x) = \epsilon_0 + \epsilon V(x), \quad (5a)$$

$$g_{22}(x) = g_{11}(x), \quad (5b)$$

$$g_{12}(x) = \eta_0 + \eta V(x) \quad (5c)$$

Here, ϵ_0 and η_0 are the homogeneous interactions associated with the background scattering length. Similarly, the ϵ and η denote the inhomogeneity interaction strength. In the present work, to investigate the sole impact of inhomogeneity, we choose $\epsilon_0 = \eta_0 = 0$ in all of our studies.

We also consider a scenario where the trapping potential (3) and spatially dependent nonlinear interactions (5a)-(5c) have a phase difference θ . With this the nonlinear interactions take the form as:

$$g_{11}(x) = -\epsilon \sum_{l=1}^2 V_l \cos(k_l x - \theta) \quad (6a)$$

$$g_{12}(x) = -\eta \sum_{l=1}^2 V_l \cos(k_l x + \theta) \quad (6b)$$

As a second case, we have chosen a spatial inhomogeneity in the interspecies interaction to be the same as that of the quasiperiodic potential but with a phase difference $\theta = \pi/2$.

The dynamical equations [Eqs. 1(a) and 1(b)] are solved using the split-step Crank-Nicholson method [63–65] with the box size as $[-102.4 : 102.4]$, space step $\Delta x = 0.025$ and time step $\Delta t = 10^{-4}$. For all the simulations, we consider the Gaussian wavefunction centered at zero as an initial state for both the components and also assume the antisymmetric condition, $\psi_1(x) = -\psi_2(-x)$ between the components. While solving the dynamical equations, we employ an imaginary-time scheme to obtain the ground state and a real-time propagation scheme for investigating the condensate dynamics.

III. RESULTS

In this section, we present the effect of the inhomogeneous interaction and the Rabi and SO coupling on the spatial profile of the ground state obtained using the imaginary time propagation. First, we focus on analyzing the impact of the inhomogeneity on the localization of the ground state. Following this, we investigate the effect of phase shift between the interaction and potential

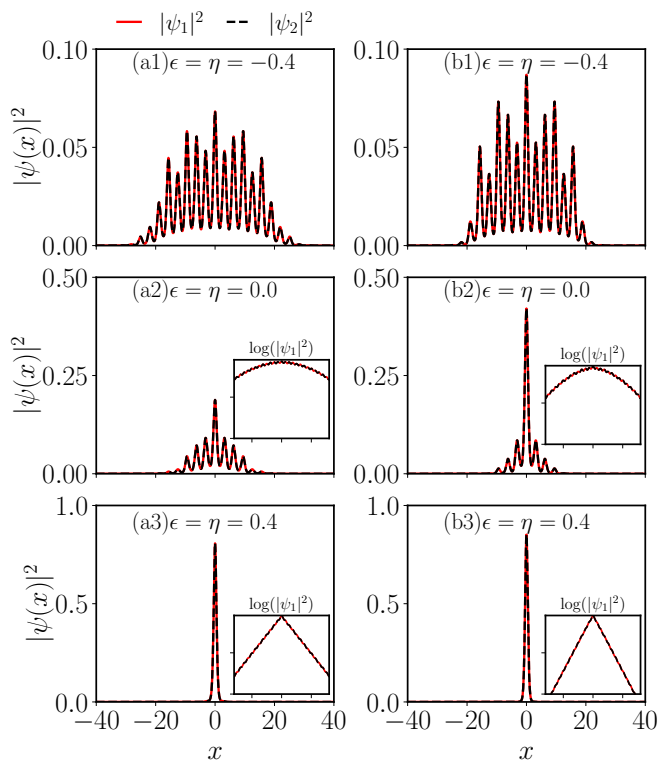


FIG. 1. Density profile of up (red line) and down (dashed black line) components for different inhomogeneity parameter $\epsilon = \eta = -0.4$ (a1,b1), $\epsilon = \eta = 0$ (a2,b2), and $\epsilon = \eta = 0.4$ (a3,b3) at $k_L = 0, \Omega = 0.0$ (left column) and $k_L = 0.6, \Omega = 1$ (right panel). Insets in [(a2, a3, b2, b3)] show the spatial variation of density profile in semilog scale that explicitly displays the exponential tail of the localized condensate in (a3) and (b3).

in bringing the interesting interplay between the localized and delocalized state that finally leads to the manifestation of the reentrant features of the localization with change in the interaction inhomogeneity. We complement our numerical observation related to the reentrant behaviour by employing the Gaussian variational approach. Finally, we present a detailed nature of the dynamics of the localized and delocalized state induced by several means, namely, by giving small velocity perturbations and quenching of the potential.

A. Effect of interaction inhomogeneity on the Localization-delocalization transition of the condensate

In a recent work [25] Li *et al.* demonstrated that the condensate remains localized for a higher ratio of secondary to the primary optical lattice strength (V_2/V_1) for all the range of SO and Rabi coupling parameters. However, for small V_2/V_1 (~ 0.1), the condensate exhibits a delocalized nature, which undergoes a transition to the localized state upon either increasing the Rabi coupling

for a fixed SO coupling or increasing the SO coupling for a fixed Rabi coupling. While in the former case, the

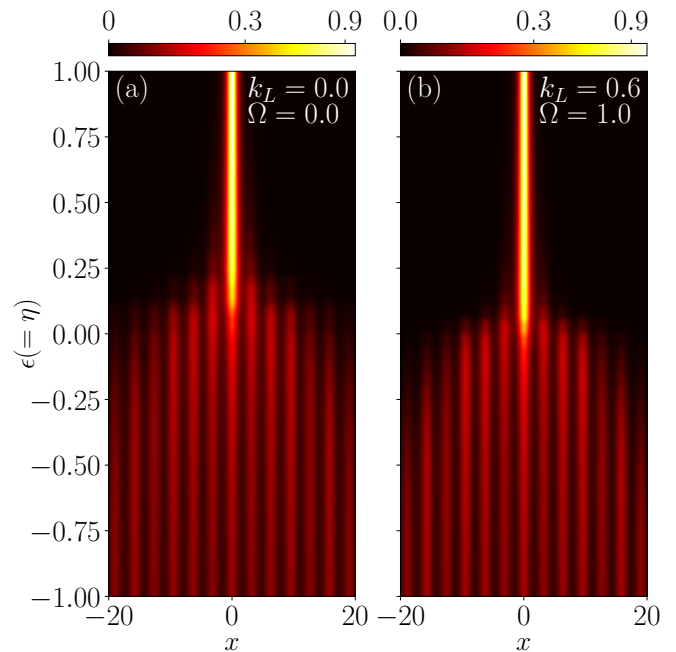


FIG. 2. Pseudo color representation of the spatial variation of ground state density of the spin-up component ($|\psi_1|^2$) with the inhomogeneity parameter $\epsilon = \eta$ for (a) $k_L = 0, \Omega = 0$ and (b) $k_L = 0.6, \Omega = 1.0$. For the zero coupling parameter, the condensate exhibits a delocalized state for $\epsilon = \eta \lesssim 0.2$ and a localized state for $\epsilon = \eta > 0.2$. However, for finite coupling parameter ($\Omega = 1, k_L = 0.6$) the localization state is realized for $\epsilon = \eta \gtrsim 0$.

condensate remains delocalized with small value of SO coupling strength, whereas, for moderate SO coupling strength the condensate remain localized at high Rabi coupling. In the latter case, it shows the reentrant nature of the localization with the change in the SO coupling for small Rabi coupling. In this work, we aim to analyze the effect of interaction inhomogeneity in tandem with the SO and Rabi coupling parameters for the state, that is, delocalized, in the absence of inhomogeneity and coupling parameters. In the following, we investigate the effect of inhomogeneity and coupling parameters on the localization state of the condensate by fixing $V_2/V_1 = 0.1$.

In Fig. 1, we show the spatial profile of the density for different sets of spatial inhomogeneity parameters by considering the coupling parameters as $\Omega = 0, k_L = 0$ (left column) and $\Omega = 1, k_L = 0.6$ (right column). In the absence of the SO and Rabi coupling, the condensate density profile exhibits a delocalized nature for zero ($\epsilon = \eta = 0$) and attractive inhomogeneity ($\epsilon = \eta = -0.4$) as depicted in the Figs. 1(a2) and (a1), respectively. The condensate starts showing a tendency to localization for the repulsive inhomogeneous interaction, quite evident with the exponential tail as shown in the inset of Fig. 1(a3). As we consider the SO and the Rabi cou-

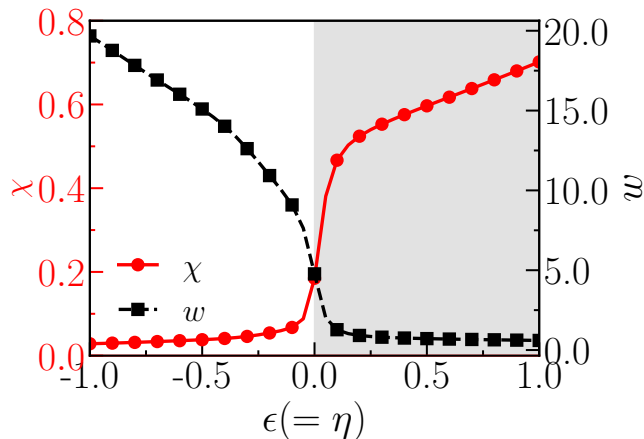


FIG. 3. The form-factor χ (red circle marked solid line) and the width w (black square marked dashed line) of the condensate as a function of inhomogeneity parameter $\epsilon(=\eta)$ for $k_L = 0.6$ and $\Omega = 1.0$. The increase in χ is accompanied by a decrease in the width of the condensate, which starts beyond the critical inhomogeneity parameter $\epsilon(=\eta) \geq 0.1$, indicating a transition from the delocalized to localized state. The localized range is shown with the grey-shaded area. Here, the left and right vertical axis shows the variation of χ and w , respectively.

plings to a finite value, we find that the spatial spread of the condensate becomes narrower compared to those with the coupling parameters for the attractive and zero inhomogeneity parameters, which is quite evident from the Fig. 1(b1) and (b2), respectively. Here, it is interesting to note that even for repulsive inhomogeneity, the condensate exhibits the localization [Fig. 1(b3)] contrary to the situation when inhomogeneity is absent. Note that, in the absence of inhomogeneity, even a small repulsive nonlinear interaction destroys the localization of the condensate [66].

To investigate the effect of inhomogeneity in a more systematic way in Fig. 2, we show the pseudocolour density profile of the condensate with a continuous variation of the inhomogeneity parameter for zero [Fig. 2(a)] and finite couplings, $\Omega = 1$ and $k_L = 0.6$ [Fig. 2(b)]. For this case, we find that the condensate remains delocalized for the attractive interaction inhomogeneity, while we witness localization for repulsive inhomogeneity interaction. The overall features indicate that for zero coupling parameters ($\Omega = k_L = 0$), the density gets localized for $\epsilon(=\eta) \gtrsim 0.2$. However, with $k_L = 0.6$ and $\Omega = 1$, the condensate display localization even without interaction inhomogeneity ($\epsilon(=\eta) \gtrsim 0$). This particular feature suggests an interplay between interaction inhomogeneity and the coupling parameters towards the localization of the condensate. On the one hand, while the attractive inhomogeneity tends to delocalize the condensate, the coupling parameters try to restore the localization. To shed more light on this aspect, in the following, we will present a systematic analysis of the role of these competing factors on delocalization, which will be connected

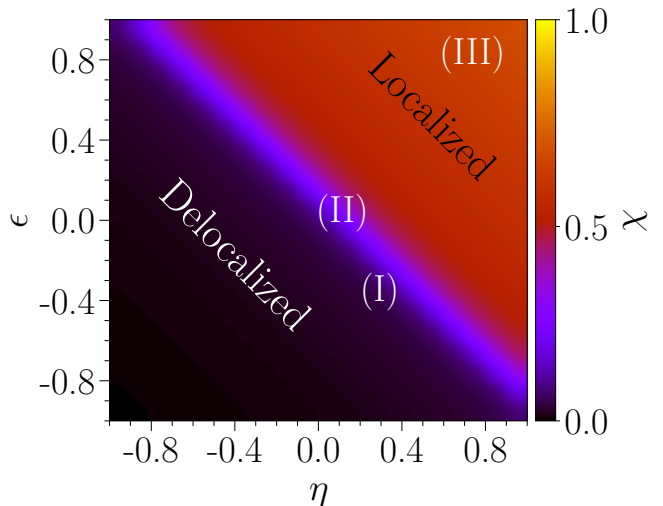


FIG. 4. Pseudo color representation of the form-factor (χ) in the $\epsilon - \eta$ plane for $k_L = 0.6$ and $\Omega = 1.0$. For $\chi \gtrsim 0.5$, the condensate is characterized in the localized state, while with $\chi < 0.5$, it is termed as delocalized. Three distinct regions, I, II, and III, represent the delocalized, intermediate localized and localized states.

further to bring the reentrant feature of the localization in the similar line observed in the many body system [49].

The extent of localization and delocalization of the condensate has been characterized using two quantities, namely, the integral form factor (χ) and the width (w) of the condensate, which are defined as [25, 49],

$$\chi_j = \frac{1}{N_j^2} \int |\psi_j|^4 dx, \quad (7a)$$

$$w_j^2 = 2 \int (x - x_m)^2 |\psi_j|^2 dx, \quad (7b)$$

where $N_j = \int_{-\infty}^{\infty} |\psi_j(x)|^2 dx$ represents the population of the j^{th} component of the condensate with $j \in \{1, 2\}$ and x_m is the center of mass of the condensate. Since we choose equal number of atoms in each component, the condensate density remains same in both components, and hence, the form factor and width can be considered as $\chi_1 = \chi_2 \equiv \chi$ and $w_1 = w_2 \equiv w$, respectively. Consequently, we show the results pertaining solely to the spin-up components only. We set the criteria that the condensate can be characterized as in the localized state if $\chi \geq 0.5$. Otherwise, for the lower form factor ($0.3 \lesssim \chi \lesssim 0.5$), the condensate is in the intermediate localized state and the delocalized state for ($\chi \lesssim 0.3$).

In Fig. 3, we illustrate the variation of the form factor (in the left vertical axis) and width (in the right vertical axis) of the condensate with respect to the change in the interaction inhomogeneity considering the equal inter- and intra- interaction ($\epsilon = \eta$). In accordance with the above discussion, we find that the χ remains close to zero for attractive interaction inhomogeneity ($\epsilon = \eta < 0$), indicating the delocalized state of the condensate and increases to $\chi \sim 0.5$ as soon as inhomogeneity gets tuned

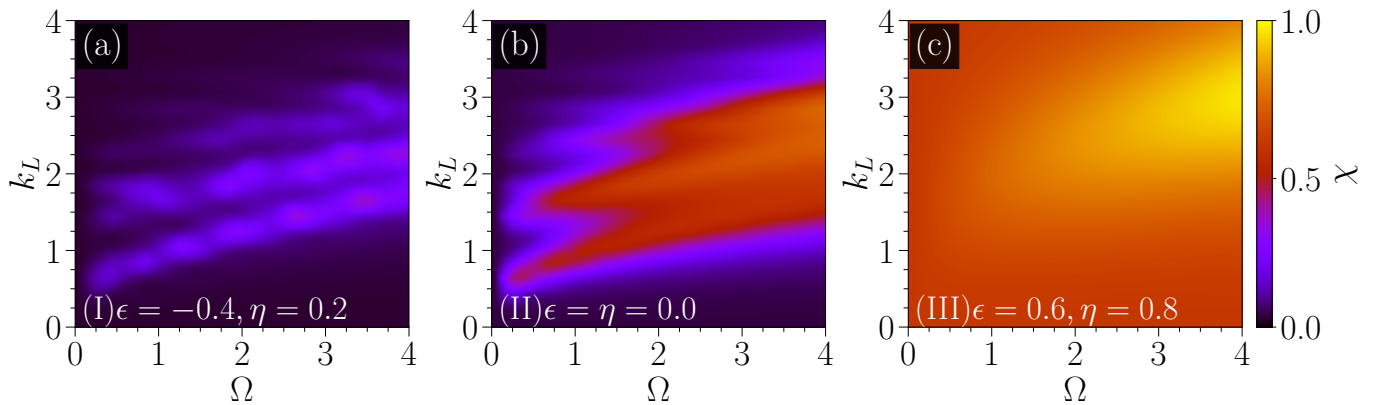


FIG. 5. Pseudo color representation of the form factor χ in $k_L - \Omega$ plane in three distinct regions of the inhomogeneity parameters as indicated in the Fig. 4: (a) for $\epsilon = -0.4$, and $\eta = 0.2$ in the region I, (b) for $\epsilon = \eta = 0.0$ in region II, and (c) for $\epsilon = 0.6, \eta = 0.8$ in region III. Regions I and III remain in the delocalized and localized states for all ranges of Ω and k_L . Region II exhibits the reentrant localization upon tuning the SO and Rabi coupling.

towards the repulsive region ($\epsilon = \eta \gtrsim 0$). This trend further continues upon increasing the interaction inhomogeneity. Overall, we find that the slightly repulsive nature of the interaction inhomogeneity is good enough to localize the condensate. This feature of χ in characterizing the localization of the condensate is very well complemented by the variation of the width (w) of the condensate as shown using the black dashed squared line in Fig. 3. The width remains high ($w \gtrsim 5$) until ($\epsilon = \eta < 0$), for which the condensate remains delocalized. In the case of the localized condensate for repulsive interactions, the condensate width becomes nearly equal to one.

To understand the effect of the interaction inhomogeneity on the localization of the condensate, we perform an extensive simulation for different ranges of interaction inhomogeneity ($|\epsilon| = |\eta| < 1$) by keeping the SO and Rabi coupling fixed at $k_L = 0.6$ and $\Omega = 1$. In Fig. 4, we present the pseudo color of form-factor χ in the $\epsilon - \eta$ plane. Here, we have used the criteria, $\chi \gtrsim 0.5$, to designate the state of the condensate as a localized state. When both intraspecies (ϵ) and interspecies (η) are positive, the condensate remains in the localized state with $\chi \gtrsim 0.6$. However, if both interactions are attractive, the form factor remains in the range $0.03 \leq \chi \leq 0.1$, indicating the delocalized state of the condensate.

Next, we present the effect of SO (k_L) and Rabi (Ω) couplings on the localization and delocalization of the condensate with spatial dependent interactions. For this analysis, we select three sets of parameters ϵ , and η of Fig. 4. These parameters are associated with three different regions: region I with $\epsilon = -0.4, \eta = 0.2$, region II with $\epsilon = \eta = 0.0$, and region III with $\epsilon = 0.6, \eta = 0.8$, as marked in Fig. 4.

In Fig. 5(a) we show the phase diagram in $k_L - \Omega$ plane for $\epsilon = -0.4$, and $\eta = 0.2$. We notice that the form factor χ remains within the range $0 \lesssim \chi \lesssim 0.4$ for all ranges k_L and Ω , revealing that the condensate still associates with the delocalized state. Fig. 5(b) illustrates the χ in the

$\Omega - k_L$ plane for the region II ($\epsilon = \eta = 0$) located at the phase boundary between the delocalized and localized phases in the $\epsilon - \eta$ plane (see Fig. 4). Furthermore, for this case, χ lies within the range $0.1 \lesssim \chi \lesssim 0.75$, implying a transition from delocalized to the localized state of the condensate. We further find the reentrant of localization as SO coupling is increased in the range $0 \leq k_L \leq 4$ while keeping Ω fixed at a low value ($\Omega \sim 1$). Similar reentrant features also have been reported earlier by Li *et al.* [25] by tuning the k_L for non-interacting condensate. After the comprehensive picture of the condensate phase in $\Omega - k_L$ plane for the non-interacting case, next, we consider repulsive inhomogeneous interactions with $\epsilon = 0.6, \eta = 0.8$ marked as region III in Fig. 4. For this case, the χ value lies within $0.60 \lesssim \chi \lesssim 1.0$, suggesting a complete localization of the condensate as shown in Fig. 5(c). Interestingly, we find that the condensate becomes strongly localized ($\chi \sim 1$) for high SO and Rabi coupling parameters, even when the interactions in the condensate are repulsive in contrast to the homogeneous interaction where the repulsive interaction weakens the localization [66]. In the second part of the paper, we will connect this enhancement of the localization with an increase in the repulsive interaction in the case of spatial inhomogeneity with the enhancement of the depth of the effective potential of the condensate using the variational approach.

B. Reentrant localization in presence of collisional inhomogeneities

In the previous section, we investigated the effect of spatially inhomogeneous interaction for the case when the spatial inhomogeneity in the nonlinear interaction is similar to those of the bichromatic lattice potential. Next, we consider the situation when there happens to be $\pi/2$ phase difference between the trapping potential and in-

homogeneous interactions as given in Eqs. (6a) and (6b). In Fig. 6(a), we present the variation of the condensate

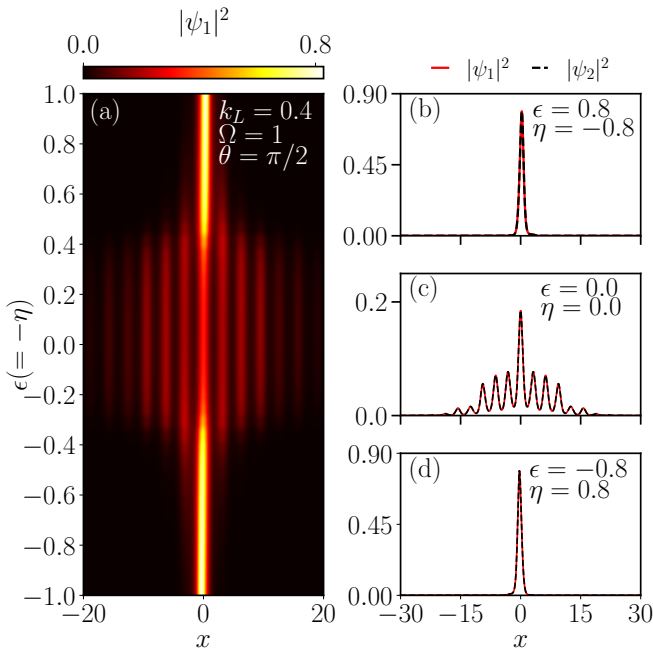


FIG. 6. Effect of inhomogeneity on the density profile of the condensate for $\pi/2$ phase difference between the nonlinearity and potential with $k_L = 0.4$ and $\Omega = 1.0$. (a) Pseudo color representation of density spatial profile with respect to the inhomogeneous interaction parameter $\epsilon(= -\eta)$. (b)-(d) spatial density profile for $\epsilon(= -\eta) = 0.8$ (localized), $\epsilon(= -\eta) = 0$ (delocalized), and (d) $\epsilon(= -\eta) = -0.8$ (localized). Reentrant localization upon increasing the strength of the inhomogeneity from the attractive to repulsive region.

density with the inhomogeneous interaction strength ϵ and η by assuming $\epsilon = -\eta$. We find that the condensate exhibits localization for $-0.4 \gtrsim \epsilon(= -\eta) \gtrsim -1.0$, $0.4 \lesssim \epsilon(= -\eta) \lesssim 1.0$ while, it displays delocalized nature $-0.4 \lesssim \epsilon(= -\eta) \lesssim 0.4$ as the coupling parameters are fixed to $k_L = 0.4$ and $\Omega = 1$. In Figs. 6(b)-(d), we show the density profile for three sets of parameters $\epsilon = -\eta = 0.8$, $\epsilon = -\eta = 0$, and $\epsilon = -\eta = -0.8$, respectively. In the case of Fig. 6(b), the condensate is localized at $x_0 \approx 0.3$, whereas in Fig. 6(d), the condensate is localized at $x_0 \approx -0.3$. The shifting of the center of mass of the condensate is explained further using the effective potential using the variational approach in Sec. III C. In contrast, Fig. 6(c) illustrates a completely delocalized phase of the condensate in the absence of inhomogeneity.

Next, to get a comprehensive picture of the localized and delocalized phases due to the effect of the inhomogeneities, we show the pseudo color representation of χ in the $\epsilon - \eta$ plane for $\Omega = 1$ and $k_L = 0.4$ in Fig. 7. We noted that the delocalized region, where the χ remains near zero, is sandwiched between two localized regions with $\chi \gtrsim 0.5$. This particular feature of localization-delocalization transition with interaction in-

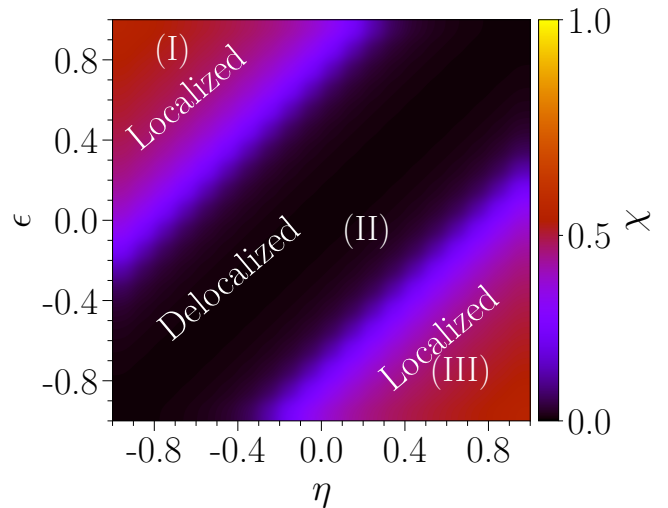


FIG. 7. Pseudo color representation of the form factor χ in the $\epsilon - \eta$ plane showing reentrant feature of the localization for $\pi/2$ phase between the inhomogeneity and potential. The parameters are $k_L = 0.4$, $\theta = \pi/2$, and $\Omega = 1.0$. Localized ($\chi \gtrsim 0.5$), intermediate localized ($0.1 < \chi \lesssim 0.5$) and delocalized ($\chi \lesssim 0.1$) have been observed. I, II, and III denote the three distinct regimes in the inhomogeneous parameters space chosen to investigate the effect of Ω and k_L on the localization and delocalization.

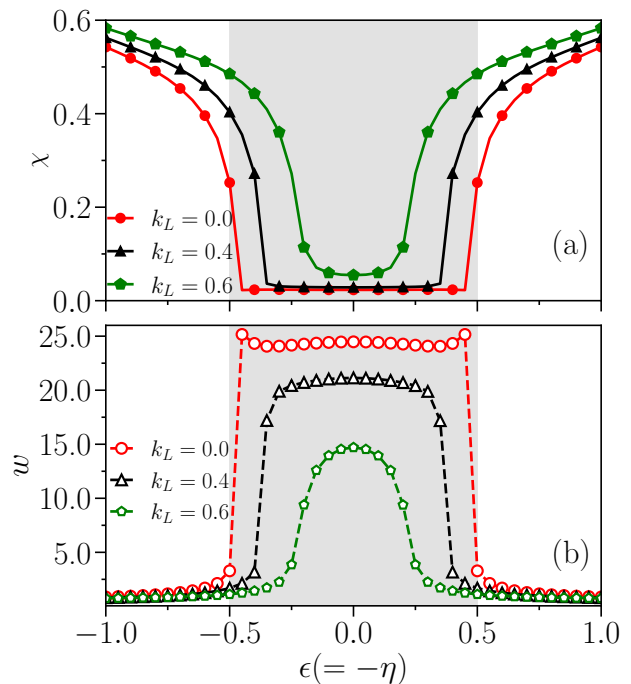


FIG. 8. Variation of (a) form-factor (χ) and (b) width (w) of the condensate as a function of the interaction inhomogeneity parameter $\epsilon = -\eta$ for $k_L = 0$ (red circles), $k_L = 0.4$ (black triangle), and $k_L = 0.6$ (green pentagons) by fixing $\Omega = 1$. Increasing k_L reduces the range of inhomogeneity parameters in which delocalization is observed.

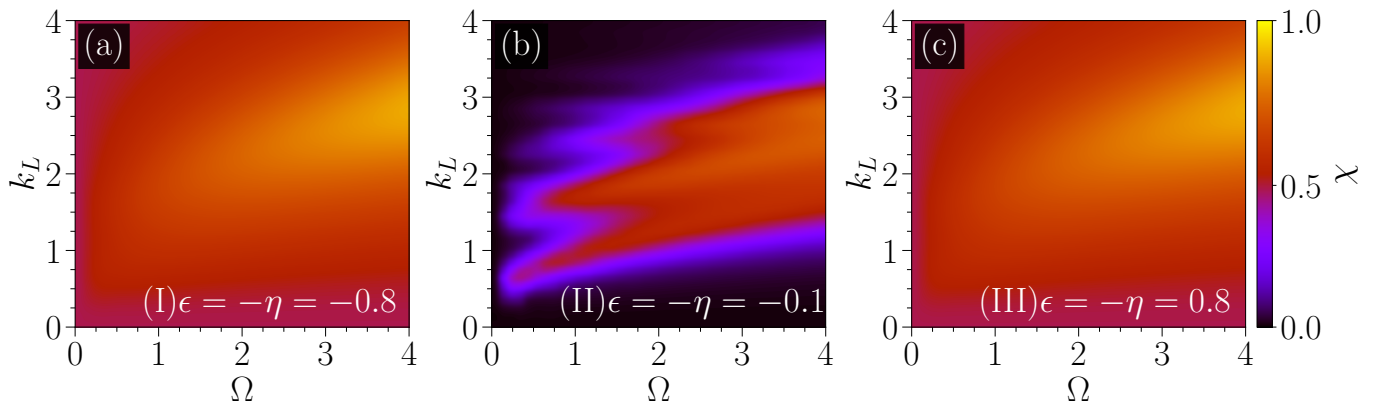


FIG. 9. Pseudo color representation of the form factor in the $\Omega - k_L$ plane in three distinct regions (I, II, and III) of interaction inhomogeneity parameter space as shown in the Fig. 7: (a) $\epsilon = -\eta = 0.8$, region I, (b) $\epsilon = -\eta = -0.1$, region II, and (c) $\epsilon = -\eta = -0.8$, region III. Both regions I and III exhibit the localization for all ranges of Ω and k_L , while region II displays reentrant localization by varying k_L for Ω close to 1.

homogeneities closely resembles the reentrant feature of localization with the previous studies using the Aubr -Andre models [49].

Further, we analyze the effect of spin-orbit coupling parameters on the reentrant localization. In Fig. 8(a), we show the variation of form factor χ with the interaction inhomogeneity $\epsilon (= -\eta)$ at three different values of $k_L = 0.0, 0.4$ and 0.6 . Conversely, Fig. 8(b) illustrates the condensate width w for the same values of k_L . In figure (a), for the case of $k_L = 0.4$, one can notice that the form factor increases between $0.4 \leq \chi \leq 0.6$ in between $\epsilon (= -\eta) \lesssim -0.5$ and $\epsilon (= -\eta) \gtrsim 0.5$, resembling the localized regions. On the other hand, the χ value remains almost constant ($\chi \sim 0$) in between $-0.5 \lesssim \epsilon (= -\eta) \lesssim 0.5$ depicting the delocalized region. Conversely, the condensate width w complements the form factor χ by showing $w \lesssim 1$ in the localized regions, and in the delocalized region, the width becomes $w \gg 1$. Another notable fact is that with the increment of k_L from zero, the minimum value of χ in the delocalized region and the maximum value in the localized region get increased. For instance, in the delocalized region, the χ value remains in the order of $\sim \mathcal{O}(10^{-2})$, whereas the localized region is featured with the larger χ value greater than > 0.5 . Also, one may notice that the delocalized region (grey shaded region) shrinks as the k_L value increases with the variation of $\epsilon (= -\eta)$. On the other hand, the condensate width w (dashed line with open markers) nicely complements the form-factor behaviour by showing a larger value of $w \gtrsim 10.0$ in delocalized region and the smaller value $w \lesssim 1.0$ in localized regions.

In order to get more comprehensive picture, we construct the phase diagram in $k_L - \Omega$ plane by keeping ϵ and η fixed at different regions, i.e., (I), (II) and (III) as shown in Fig. 7. The phase diagram in Fig. 9(a) corresponds to the localized region at (I) ($\epsilon = -\eta = 0.8$) where the χ value lies within the range $0.49 \lesssim \chi \lesssim 0.88$, clearly demonstrating the localized feature of the condensate.

On the other hand, when we decrease the interaction parameters towards delocalized region such as region (II) ($\epsilon = -\eta = -0.1$), the associated form-factor in Fig. 9(b) exhibits similar reentrant phenomenon as shown previously in Fig. 5(b). Next, Fig. 9(c) corresponds to the region (III) ($\epsilon = -\eta = -0.8$), which shows the localized condensate for all the range of coupling parameters.

So far, our investigations have mainly focused on numerical analysis through which we have characterized various localized and delocalized regions with variations in interactions as well as the coupling strength of the system. To understand reentrant localization, either by tuning the coupling parameters or changing the interaction strengths, we adopt the Gaussian variational approach in the following.

C. Role of inhomogeneity in the reentrant of localization

In this section, using the variation approach, we present a plausible explanation for the observation of reentrant localization obtained using the numerical simulation, as presented in Sec. III B. In what follows, we discuss the analytical model using the variational approach to disentangle the role of different localizing and delocalizing factors in spatially inhomogeneous SO coupled BECs.

1. Variational analysis

Using the time-dependent variational approach [24], the Lagrangian density of Eqs. (1a) and (1b) can be writ-

ten as,

$$\mathcal{L} = \sum_{j=1}^2 \left\{ \frac{i}{2} (\psi_j^* \dot{\psi}_j - \dot{\psi}_j \psi_j^*) - (-1)^j \frac{i}{2} k_L [\psi_j^* \dot{\psi}_j' - \dot{\psi}_j' (\psi_j^*)'] \right. \\ \left. - \frac{1}{2} |\dot{\psi}_j'|^2 - \frac{1}{2} g(x) |\psi_j|^4 - V(x) |\psi_j|^2 \right\} \\ - g_{12}(x) |\psi_1|^2 |\psi_2|^2 - \Omega (\psi_1^* \psi_2 + \psi_1 \psi_2^*) \quad (8)$$

where asterisk denotes the complex conjugate, prime represents the derivative (d/dx), and overdot denotes the time derivative (d/dt). Here, the notation $j = 1$ and 2 refers to the spin-up and spin-down components, respectively.

To obtain the corresponding dynamical equations, we use the Gaussian ansatz with time-dependent variational parameters N_j , w_j , β_j , x_{0_j} and ϕ_j of the form:

$$\psi_j(x, t) = \frac{1}{\pi^{1/4}} \sqrt{\frac{N_j}{w_j}} \exp \left[-\frac{(x - x_{0_j})^2}{2w_j^2} \right] \\ \times \exp \left[(-1)^j i \beta_j (x - x_{0_j}) + i \phi_j \right], \quad (9)$$

where N_j is the number of atoms, w_j represents the width of the condensate centered at x_{0_j} , β_j and ϕ_j are respectively the chirp and phase of the condensate with Gaussian profile. The effective Lagrangian with the Gaussian ansatz can be obtained by substituting Eq. (9) into Eq. (8) and integrating over space variable with the potential Eq. (3) and the nonlinearity Eq. (5). The detailed calculation for the dynamical equation of motion using the Lagrangian is given in Appendix A.

First, we focus on analyzing the stationary state upon solving the coupled equations (Eq. 1a and Eq. 1b) considering equal atoms in both components (i.e., $N_1 = N_2$). In order to obtain the stationary conditions, we need to make the time derivative of Eqs.(A2b–A2d) is equal to zero. As a result, we obtain $\beta_1 = \beta_2 = \beta$, $w_1 = w_2 = w$, and $x_{0_1} = -x_{0_2} = x_0$ as the initial condition. Using these initial conditions, the equations of motion associated to x_0 , w and β have the form,

$$k_L - \beta - \sqrt{\frac{N_{3-j}}{N_j}} \frac{\partial L_\Omega}{\partial \beta_j} = 0 \quad (10a)$$

$$\frac{1}{2w^3} + \frac{1}{2\sqrt{2\pi}w^2} \left[\epsilon_0 - \frac{\epsilon}{4} \sum_{l=1}^2 V_l (k_l^2 w^2 + 4) \exp \left(-\frac{k_l^2 w^2}{8} \right) \times \cos(k_l x_0) \right] - \frac{w}{2} \sum_{l=1}^2 (V_l k_l^2) \cos(k_l x_0) \exp \left(-\frac{k_l^2 w^2}{4} \right) \\ + \frac{\eta_0}{2\sqrt{2\pi}w^4} (w^2 - 4x_0^2) \exp \left(-\frac{2x_0^2}{w^2} \right) - \frac{\eta}{2\sqrt{2\pi}w^4} \sum_{l=1}^2 V_l \left(-4x_0^2 + w^2 + \frac{k_l^2 w^4}{4} \right) \exp \left(-\frac{k_l^2 w^2}{8} \right) \\ + 2\Omega \exp \left(-\frac{x_0^2 + \beta^2 w^4}{w^2} \right) \left(\beta^2 w + \frac{x_0^2}{w^3} \right) = 0 \quad (10b)$$

$$\frac{(-1)^{j-1} N_j \epsilon}{2\sqrt{2\pi}w} \sum_{l=1}^2 (V_l k_l) \sin(k_l x_0) \exp \left(-\frac{k_l^2 w^2}{8} \right) + \sum_{l=1}^2 (V_l k_l) \sin(k_l x_0) \exp \left(-\frac{k_l^2 w^2}{4} \right) - \frac{\sqrt{2}\eta_0 N_{3-j} x_0}{\sqrt{\pi}w^3} \\ \times \exp \left(-\frac{2x_0^2}{w^2} \right) - \frac{(-1)^{2j-1} \eta N_{3-j}}{2^{3/2} \sqrt{\pi}w^3} \exp \left(-\frac{2x_0^2}{w^2} \right) \sum_{l=1}^2 (-1)^j 4V_l x_0 \exp \left(-\frac{k_l^2 w^2}{8} \right) + \sqrt{\frac{N_{3-j}}{N_j}} (-1)^{j-1} \frac{\partial L_\Omega}{\partial x_{0_j}} = 0 \quad (10c)$$

In Fig. 10 we show a comparison between the density profile of spin-up component obtained using GPE (with solid line) and that using the variational approach [Eq. (10a)–(10c)] shown with open markers considering $k_L = 0.91$, $\epsilon = \eta = 0$, and $\Omega = 1.0$ [see Fig. 10(a)], and $\epsilon = \eta = 0.4$, $k_L = 0.6$ and $\Omega = 1.0$ [see Fig. 10(b)]. At stationary state, $|\psi_1|^2 = |\psi_2|^2$, $\text{Im} \psi_1 = \text{Im} \psi_2$, and

$\text{Re} \psi_1 = -\text{Re} \psi_2$. Noting this, hereafter, we consider the spin-up component for the discussion. The density profile calculated using the numerical GPE and variational approach agree well in the localized state. For the non-interacting case ($\epsilon = \eta = 0$), the variational approach (Eq. (10b)) reveals that the kinetic energy (first term) is responsible for the delocalization. However, the

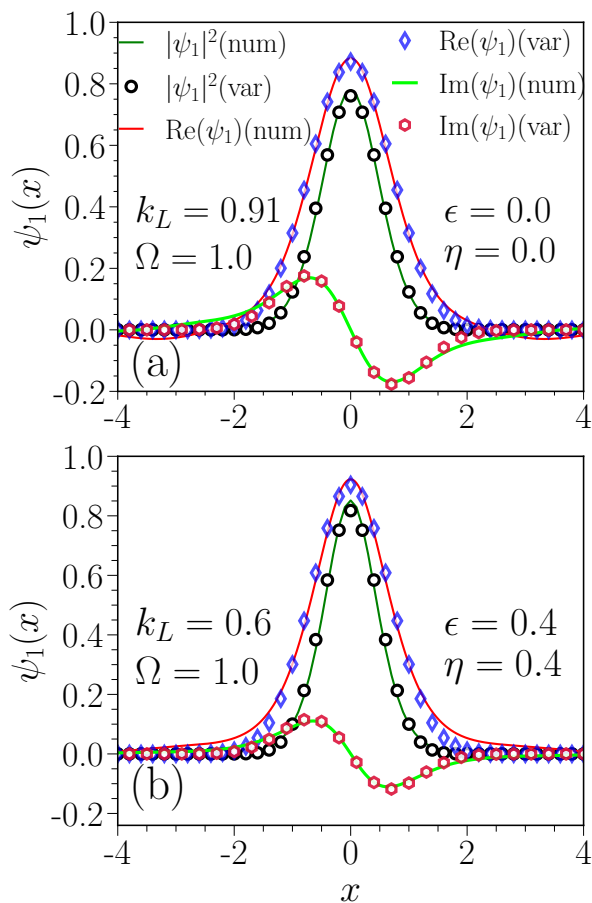


FIG. 10. Ground state density profile obtained using numerical (with lines) and variational scheme (with markers) for (a) $k_L = 0.91$, $\epsilon(= \eta) = 0$, and (b) $k_L = 0.6$, $\epsilon(= \eta) = 0.4$. The real and imaginary parts of the spin-up condensate wavefunction obtained from the numerical simulation and variational approach agree well.

Rabi-coupling and the optical lattice potential contribute to localization of the condensate, which is in line with the observations made earlier (refer to the discussion in Sec. III A). Further, to highlight the effect of inhomogeneities on the localization in Fig. 10(b), we illustrate the density profile for $\epsilon = \eta = 0.4$, $k_L = 0.6$ and $\Omega = 1.0$. The density profile obtained using the variational approach agrees well with those obtained using GPE with slightly higher amplitude than those for non-interacting cases, indicating a stronger localization with repulsive nonlinearity.

In Fig. 11 we show the variation of total energy (E_{total}) with interaction inhomogeneity as ($\epsilon = \eta$). For attractive interaction ($\epsilon = \eta \leq 0$), the total energy calculated using numerics remains constant at $E_{\text{num}} = -2.5$. On the other hand, for repulsive interactions ($\epsilon(= \eta) \geq 0$), the E_{num} decreases monotonically upon increasing interaction strength, indicating that the localized condensate minimizes the energy. However, the total energy E_{var} calculated using the variational approach agrees well in

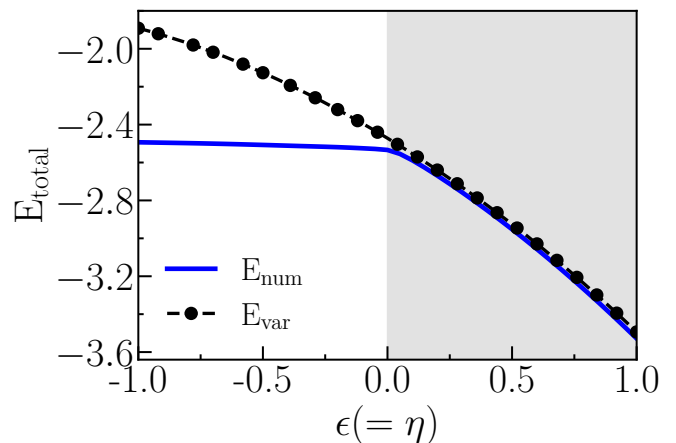


FIG. 11. Variation of the ground state energy as a function of the inhomogeneity parameter ($\epsilon = \eta$). E_{num} (solid-blue line) and E_{var} (dashed line with dots) represent the total energy obtained from numerical simulation and analytical variational approach, respectively. Here $k_L = 0.6$ and $\Omega = 1$. There is good agreement between the numerical and variational energy in the localized region ($\epsilon = \eta > 0$) where energy increases towards more negative, indicating the formation of stronger localization with an increase in the inhomogeneity. In the delocalized region, $E_{\text{num}} \sim -2.5$ for negative inhomogeneity parameter.

the localized region with numerics.

The localization appears to arise from the interplay between interactions and the bichromatic optical lattice in a collisionally inhomogeneous environment. To account for this, we consider a phase difference of $\theta = \pi/2$ between the interaction and the potential, as given in Eqs. (6a) and (6b), respectively, which we further substitute into the Lagrangian (Eq. (8)). Using the Euler-Lagrange formalism, we calculate the equations of motion with respect to the variational parameters. The details of the Lagrangian are provided in Appendix B.

2. Effective Potential for reentrant localization

To understand the role of inhomogeneity in the localization of the condensate, we resort to derive the dynamical equation of the condensate moving under the influence of effective potential mainly generated due to the spatial inhomogeneity [34, 35].

The effective potential can be obtained using Eq. (A2c) and Eq. (A2e) (see Appendix A and B for details), which yields:

$$\frac{\partial^2 x_{0j}}{\partial t^2} = -\dot{\beta}_j = -\frac{\partial V_j^{\text{eff}}}{\partial x_{0j}} \quad (11)$$

In Fig. 12(a), we show the profile of V_{eff} corresponding to the spin-up component upon varying the inhomogeneous interactions while keeping the intra and intercomponent interaction same for $k_L = 0.6$ and $\Omega = 1$. We

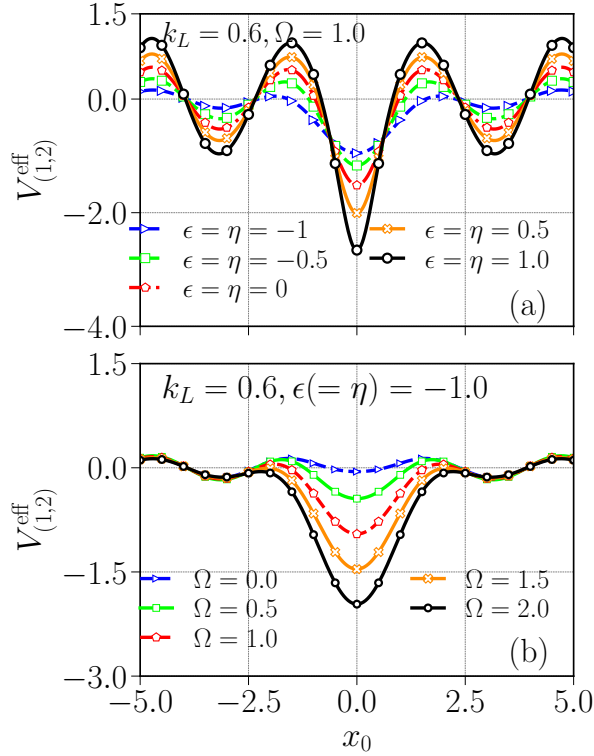


FIG. 12. Effective potential ($V_{(1,2)}^{\text{eff}}$) profile for the condensate obtained using variational approach [Eq. A3a]: (a) for different inhomogeneous interaction parameter keeping $\Omega = 1$ and $k_L = 0.6$ and (b) for different Ω keeping $k_L = 0.6$ and inhomogeneity interaction as $\epsilon(= \eta) = -1.0$. The depth of the effective potential at the central point ($x_0 \sim 0$) increases upon increasing the repulsive interaction compared to those for $\epsilon = \eta = 0$ indicating the localization for the condensate for repulsive interaction inhomogeneity. However, the trend is opposite for an increase in the attractive interaction, implying the delocalization for them. Upon an increase of Ω in (b), the central depth increases, suggesting the localization of condensate for this increment.

find that the effective potential attains a global minimum at $x_0 = 0$, and the depth of the global minimum increases upon an increase in the spatial repulsive inhomogeneous interaction. For instance, at $\epsilon = \eta = 1$ (open circled black solid line), a larger depth of effective potential ($V_{\text{eff}} \sim 2.5$) indicates that the condensate gets more localized as the repulsive interaction increased. However, for attractive interaction (ϵ or $\eta < 0$), the depth of minima at $x_0 \sim 0$ becomes of the order of other minima of the effective potential, indicating the delocalized state of the condensate. This observation aligns with the earlier numerical results obtained with the one component BECs [35]. Additionally, this result closely matches the observed transition from localized to delocalized states when interaction parameters are varied from positive to negative (see Fig. 3).

In the similar line as discussed above, to understand the role of Rabi coupling in attaining the localization, we show the effective potential in Fig. 12(b) as Ω is increased

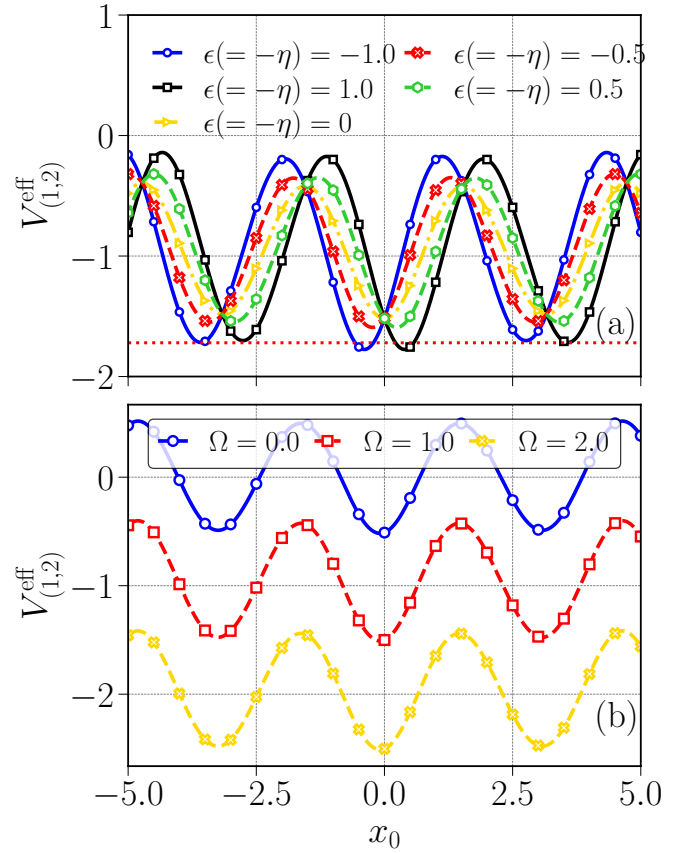


FIG. 13. (a) Variation of effective potential ($V_{(1,2)}^{\text{eff}}$) as obtained in Eq. B1b of spin-components with x_0 for different inhomogeneous interaction parameters $\epsilon(= -\eta)$ when the phase difference between the spatial inhomogeneity and potential considered is $\pi/2$. For $\epsilon = \eta = 0$, the potential is peaked at $x_0 = 0$, which is the delocalized state. However, for $|\epsilon(-\eta)| = 0.5$ and 1 , the central minima depth increases compared to those for zero inhomogeneity, indicating the localization state. (b) Variation of effective potential with x_0 for different Ω with $k_L = 0.6$, $\epsilon = \eta = 0$. As the value of Ω increases, the depth of the central potential also increases, implying that the Rabi coupling contributes towards the localization of the condensate.

for the condensate with $\epsilon = \eta = -1$ and $k_L = 0.6$. For $\Omega = 0$, the minima of the effective potential at $x_0 = 0$ is of the same width as of minima at other x_0 , indicating the delocalized state of the condensate. As the Rabi-coupling increased from zero, the depth of effective potential at $x_0 = 0$ increases and becomes significantly higher compared to the minima at other x_0 for $\Omega \gtrsim 0.5$. This variation of the effective potential with increasing Ω indicates that the role of Rabi coupling is to localize the condensate in the presence of inhomogeneous interaction where it was initially delocalized in line with the numerical observation made in the Sec. III A.

Next, we turn our focus on analyzing the role of spatial inhomogeneity on the reentrant localization that arises when the inhomogeneous nonlinear interaction car-

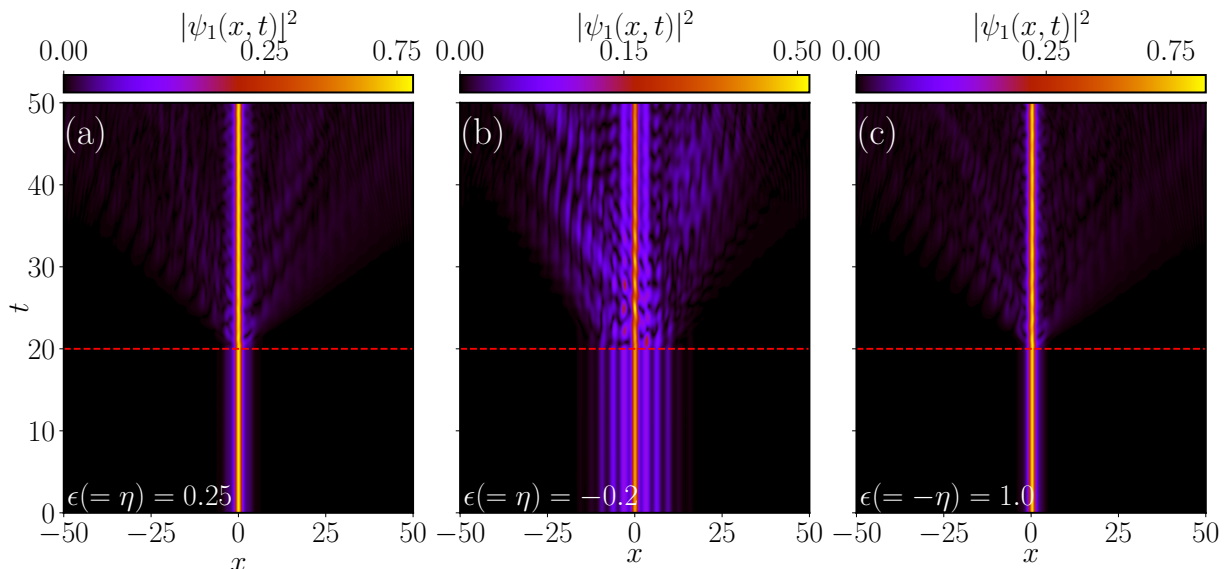


FIG. 14. Pseudo color representation of the velocity-induced dynamics of the spin-up component density for localized (a) and delocalized (b) state of the case when the inhomogeneity has the same phase as the potential. (c) shows the localized state for the case when the inhomogeneous interaction and potential have $\pi/2$ phase difference. The other parameters are $k_L = 0.6$ and $\Omega = 1$. Both the localized states (a) and (c) do not show any change in shape and size upon perturbing with the velocity, while the delocalized state (b) shows the spread in shape with time.

ries the $\pi/2$ phase difference in spatial dependence as those for the trapping quasiperiodic potential as described in Sec. III B. The form of the effective potential is provided in Appendix B.

Interestingly, the spatial variation of the effective potential in Fig. 13(a) vividly illustrates the shifting of the minima with the increment of nonlinear interactions $\epsilon(= -\eta)$ as a result of the captivating interplay between the potential and spatial dependence of the interaction. For instance, as we move from $\epsilon = \eta = 0$, the local minima at $x_0 = 0$ shifts either in the direction of positive or negative x_0 , as depicted for $\epsilon = -\eta = 0.2$ (green dashed line) or $\epsilon = -\eta = -0.2$ (purple dashed line), respectively. Notably, the displacement of the minima occurs symmetrically on both sides of the center. For example, at $\epsilon(= -\eta) = 1.0$, the minima are displaced around $x_0 = 0.3$, whereas at $\epsilon(= -\eta) = -1.0$, the minima are found to be at $x_0 = -0.3$. Also, the presence of disorder in the potential leads to a slightly larger depth of the potential well located at $x_0 = \pm 0.3$ compared to the other wells for the aforementioned interactions, which is clearly distinguishable by the red dotted line in the figure. These particular features highlight intriguing competition between the potential and nonlinearity towards the reentrant localization. Additionally, the effect of Rabi-coupling towards localization is clearly evident when studying the magnitude of V_{eff} in Fig. 13(b).

D. Effect of spatial inhomogeneity on the dynamics of localized and delocalized states

So far, we have analyzed the effect of the SO and Rabi coupling along with the interaction inhomogeneity on the localization of the condensate and studied their role using the variational approach. In this section, we present the dynamics of those localized and delocalized states by perturbing the ground state through velocity or performing a quench on the strength of the secondary potential.

1. Velocity perturbed Dynamics

In this section, we present the dynamics that ensued in the condensate as a result of the finite equal and opposite velocity imparted to the condensate in the localized or delocalized state in the presence of the interaction inhomogeneities. After imparting the velocity, we analyze the condensate dynamics utilizing the real-time propagation scheme.

In Fig. 14, we show the temporal evolution of spin-up component condensate density for various interaction inhomogeneities. In panel (a), we observe the initial localized state obtained when the phase between spatial inhomogeneity and potential is zero ($\theta = 0$), with parameters $\epsilon = \eta = 0.2$, $k_L = 0.6$, and $\Omega = 1.0$. After applying a velocity perturbation at $t = 20$, we observe a slight change in the condensate. Only a small fraction generates ripples in space, while the maximum density remains almost unchanged compared to the ground state density. A similar behaviour is observed for the localized condensate when

the phase shift is $\theta = \pi/2$, $\epsilon(= -\eta) = 1.0$ (see panel (c)). In panel (b), the delocalized condensate density demonstrates expansion in space over time after the velocity perturbation at $t = 20$ (after the red dashed line). In summary, it can be said that localized condensates [see Fig. 14(a) and Fig. 14(c)] remain stable against small perturbations, while delocalized condensates [see Fig. 14(b)] exhibit instability under similar perturbations [35].

2. Quench induced dynamics

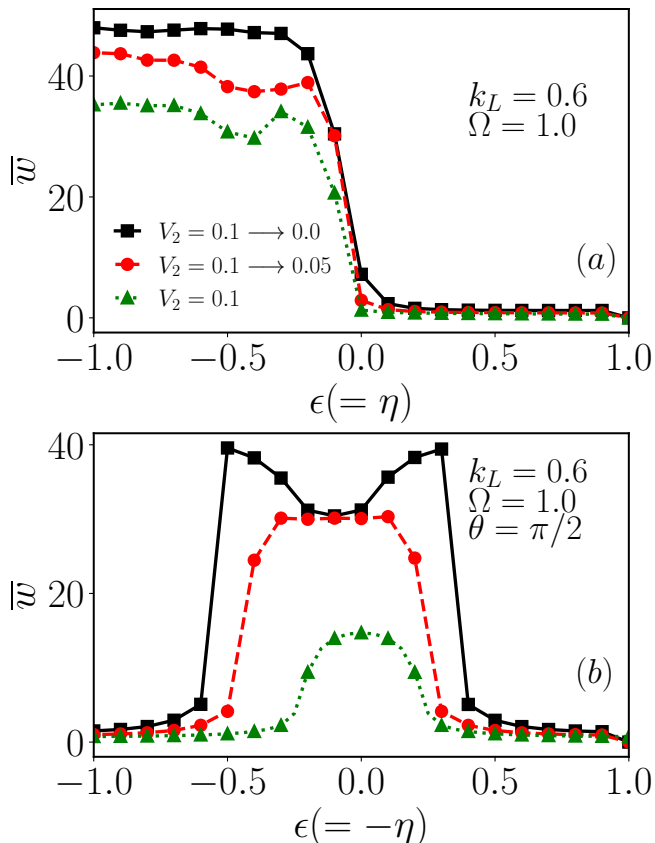


FIG. 15. Time averaged mean-width (\bar{w}) of the condensate as a function of the inhomogeneity ($\epsilon = -\eta$) for different quenching of the secondary potential (V_2) from initial value 0.1 to the final value 0.0 (black rectangle) and 0.05 (red dots). Green triangle represents the case when $V_2 = 0.1$. The other parameters are $k_L = 0.6$, and $\Omega = 1.0$. For the case (a) when the inhomogeneity and potential have the same phase and (b) when the phase between the potential and nonlinear inhomogeneity is $\pi/2$.

Apart from the analysis of the localized and delocalized phases depending upon the ground state density with various coupling and interactions, now in this section, we explore the dynamics of the different phases of the condensate upon quenching of trap potentials [67–69]. Firstly, we analyze the dynamics generated by applying the quench of the trap potential from initial to different fi-

nal strength. In Fig. 15, we show the temporal average of the condensate width $\bar{w} = 1/T \int_0^T w(t) dt$, for quenching of the potential from initial ($V_2 = 0.1$) to lower trapping strength. In Fig. 15(a) we show the variation of mean width with $\epsilon(= \eta)$ as the dynamics are generated through two types of quenching: (i) by quenching the secondary lattice strength $V_2 = 0.1 \rightarrow 0.0$ (black solid line with square markers) and (ii) by quenching $V_2 = 0.1 \rightarrow 0.05$ (red dashed line with circular markers). We also show the \bar{w} (green dotted line with triangular markers) corresponding to the ground state condensate. We find that for repulsive interaction $\epsilon(= \eta) > 0$, the \bar{w} is of the same order compared to the \bar{w} obtained without quenching. This particular feature implies that the condensate stability in the localized region is primarily caused by the repulsive inhomogeneity present in the system [35]. On the other hand, with attractive interaction ($\epsilon(= \eta) < 0$), the \bar{w} tend to increase towards a larger value to the order of $\bar{w} \sim \mathcal{O}(10^1)$. Moreover, in the case of periodic quenching (when final $V_2 = 0$), the mean width is higher compared to the case of quasiperiodic quenching (when $V_2 = 0.05$), which indicates that even a low but finite disorder is good enough to resist the expansion.

In Fig. 15(b), we present the mean condensate width with the variation of $\epsilon(= -\eta)$ in the presence of the phase shift $\theta = \pi/2$. Similar to $\theta = 0$ here also, we observe that in the localized region, \bar{w} remains almost constant at the same order, $\mathcal{O}(10^{-1})$, irrespective of the strength of quenching of the trap. However in the delocalized region, the \bar{w} follows similar behavior as observed for $\theta = 0$ (See Fig. 15(a)). In general, we find that the periodic quenching (final $V_2 = 0$) results in attaining the higher \bar{w} compared to those for quasiperiodic quenching (final $V_2 = 0.05$). We also notice a slight shift of the delocalized regions towards the left side of $\epsilon(= -\eta) < 0$ for the delocalized regions compare to the case of without quenching (dotted line with green triangles). This feature can be attributed to the comparatively weak localization of the condensate with phase shift $\pi/2$ compared to the localization without phase shift. We also find the manifestation of the reentrant of the localization with a change in inhomogeneity in the dynamics of the condensate captured through the variation of the mean condensate width in Fig. 15(b) in comparison to the results obtained using ground state in Fig. 8(b).

IV. CONCLUSION

We have numerically investigated the effect of interaction inhomogeneity on the localization-delocalization transition of the SO coupled binary quasi-one dimensional BECs trapped in the quasiperiodic potentials. By assuming the form of the spatial modulation of the interaction inhomogeneity same as that of the quasiperiodic potential we have shown that the condensed undergoes a localization to delocalization transition as the inhomogeneous interaction strength varies from attractive to re-

pulsive. However, when a phase difference of $\pi/2$ is introduced between the inhomogeneity and the lattice potential, we have shown a remarkable reentrant localization transition as a function of the inhomogeneity strength. Furthermore, we have also analyzed the effect of the SO and the Rabi coupling on the localization-delocalization transition for different strength of the inhomogeneity. For weak inhomogeneity strength, the increase in the SO coupling strength leads to a reentrant localization similar to the one observed for non-interacting homogeneous SO coupled BECs [25].

Furthermore, we have utilized the variational approach to understand the competing nature of the quasiperiodic disorder due to the inhomogeneity and the potential responsible for the reentrant localization, which is revealed clearly in the oscillatory nature of the depth of the effective potential as a function of the inhomogeneity strength. We have also demonstrated the manifestation of the reentrant localization in the quench dynamics of the condensate. Our present analysis provides an alternate disorder parameter other than the external potential to attain the reentrant localization, which may motivate future experiments in BECs.

In the present work, we have considered the equal in-

traspecies interaction between the components that restrict the same population among the components. It would be intriguing to extend the formalism developed in the present work to account for the effect of unequal intraspecies interactions on the localization and delocalization of the individual component(s). Another extension would include a completely random disordered potential, where the condensate could exhibit complex phases in the localized and delocalized state.

ACKNOWLEDGMENTS

R.R. acknowledges the postdoctoral fellowship supported by Zhejiang Normal University, China, under Grants No. YS304023964. T.M. acknowledges support from Science and Engineering Research Board (SERB), Govt. of India, through project No. MTR/2022/000382 and STR/2022/000023. The work of P.M. is supported by MoE RUSA 2.0 (Bharathidasan University - Physical Sciences). We gratefully acknowledge our supercomputing facility Param-Ishan and Param Kamrupa (IITG), where all the simulation runs were performed.

Appendix A: Details of the Variational approach Calculation

In this appendix, we provide the detailed steps of time dependent variational approach. The Lagrangian for the zero phase difference between the inhomogeneous interaction and potential is given by

$$\begin{aligned}
L = & \sum_{j=1}^2 \left[N_j (-1)^j \beta_j \dot{x}_{0_j} - N_j \dot{\phi}_j + N_j \beta_j k_L - \frac{N_j}{2} \left(\frac{1}{2w_j^2} + \beta_j^2 \right) - \frac{N_j}{2^{3/2} \sqrt{\pi} w_j} \left[\epsilon_0 - \epsilon \sum_{l=1}^2 V_l \cos(k_l x_{0_j}) \exp\left(-\frac{k_l^2 w_j^2}{8}\right) \right] \right. \\
& \left. + N_j \sum_{l=1}^2 V_l \cos(k_l x_{0_j}) \exp\left(-\frac{k_l^2 w_j^2}{4}\right) \right] - \frac{N_1 N_2}{\sqrt{\pi} \sqrt{w_1^2 + w_2^2}} \exp\left(-\frac{(x_{01} - x_{02})^2}{w_1^2 + w_2^2}\right) \\
& \times \left[\eta_0 - \eta \sum_{l=1}^2 V_l \cos\left(\frac{k_l (w_1^2 x_{0_2} + w_2^2 x_{0_1})}{w_1^2 + w_2^2}\right) \exp\left(-\frac{k_l^2 w_1^2 w_2^2}{4(w_1^2 + w_2^2)}\right) \right] - 2\sqrt{N_1 N_2} L_\Omega, \tag{A1a}
\end{aligned}$$

where

$$L_\Omega = \Omega \sqrt{\frac{2w_1 w_2}{(w_1^2 + w_2^2)}} \cos \left[\frac{(\beta_1 w_1^2 - \beta_2 w_2^2) (x_{0_1} - x_{0_2}) - \phi (w_1^2 + w_2^2)}{w_1^2 + w_2^2} \right] \exp \left(-\frac{(x_{0_1} - x_{0_2})^2 + (\beta_1 + \beta_2)^2 w_1^2 w_2^2}{2(w_1^2 + w_2^2)} \right) \tag{A1b}$$

with $\phi = \phi_2 - \phi_1$, and $\rho = x_{0_1} - x_{0_2}$. The Euler-Lagrangian equation associated to variational parameters α_j is given by

$$\frac{\partial L}{\partial \alpha_j} - \frac{d}{dt} \frac{\partial L}{\partial \dot{\alpha}_j} = 0 \tag{A2a}$$

where α_j corresponds to the variational parameters N_j , β_j , ϕ_j , x_{0j} , and w_j . The Euler equation of motion corresponding to ϕ_j is given by

$$\begin{aligned} \dot{\phi}_j = & -\frac{1}{4w_j^2} + \frac{\beta_j^2}{2} - \frac{N_j}{\sqrt{2\pi}w_j} \left[\epsilon_0 - \epsilon \sum_{l=1}^2 V_l \cos(k_l x_{0j}) \exp\left(-\frac{k_l^2 w_j^2}{8}\right) \right] - \frac{N_{3-j}}{\sqrt{\pi}(w_1^2 + w_2^2)} \exp\left(-\frac{(x_{01} - x_{02})^2}{w_1^2 + w_2^2}\right) \\ & \left[\eta_0 - \eta \sum_{l=1}^2 V_l \cos\left(k_l \frac{w_1^2 x_{02} + w_2^2 x_{01}}{w_1^2 + w_2^2}\right) \exp\left(-\frac{k_l^2 w_1^2 w_2^2}{4(w_1^2 + w_2^2)}\right) \right] - \sqrt{\frac{N_{3-j}}{N_j}} L_\Omega + \beta_j \sqrt{\frac{N_{3-j}}{N_j}} \frac{\partial L_\Omega}{\partial \beta_j} \\ & + \sum_{l=1}^2 V_l \cos(k_l x_{0j}) \exp\left(-\frac{k_l^2 w_j^2}{4}\right) \end{aligned} \quad (\text{A2b})$$

In the similar line the equation of motion associated to x_{0j} is given by

$$\dot{x}_{0j} = (-1)^{1-j} \left[-k_L + \beta_j + \sqrt{\frac{N_{3-j}}{N_j}} \frac{\partial L_\Omega}{\partial \beta_j} \right] \quad (\text{A2c})$$

Further the equation of motion associated to N_j can be written as:

$$\dot{N}_j = (-1)^j 2\Omega \sqrt{N_1 N_2} \sqrt{\frac{2w_1 w_2}{w_1^2 + w_2^2}} \sin \left[\frac{(\beta_1 w_1^2 - \beta_2 w_2^2)(x_{01} - x_{02})}{(w_1^2 + w_2^2)} - \phi \right] \exp \left[-\frac{(x_{01} - x_{02})^2 + (\beta_1 + \beta_2)^2 w_1^2 w_2^2}{2(w_1^2 + w_2^2)} \right] \quad (\text{A2d})$$

The Euler equation of motion corresponding to β_j has the form as

$$\begin{aligned} \dot{\beta}_j = & \frac{N_j \epsilon}{(-1)^{3-j} 2\sqrt{2\pi}w_j} \sum_{l=1}^2 (V_l k_l) \sin(k_l x_{0j}) \exp\left(-\frac{k_l^2 w_j^2}{8}\right) + \frac{1}{(-1)^{3-j}} \sum_{l=1}^2 (V_l k_l) \sin(k_l x_{0j}) \exp\left(-\frac{k_l^2 w_j^2}{4}\right) \\ & - \frac{2\eta_0 N_{3-j} (x_{01} - x_{02})}{\sqrt{\pi}(w_1^2 + w_2^2)^{3/2}} \exp\left(-\frac{(x_{01} - x_{02})^2}{w_1^2 + w_2^2}\right) - \frac{\eta N_{3-j} (-1)^{j-3}}{\sqrt{\pi}(w_1^2 + w_2^2)^{3/2}} \exp\left(-\frac{(x_{01} - x_{02})^2}{w_1^2 + w_2^2}\right) \\ & \sum_{l=1}^2 V_l \left[(-k_l w_{3-j}^2) \sin\left(k_l \frac{w_1^2 x_{02} + w_2^2 x_{01}}{w_1^2 + w_2^2}\right) + (-1)^j 2(x_{01} - x_{02}) \cos\left(k_l \frac{w_1^2 x_{02} + w_2^2 x_{01}}{w_1^2 + w_2^2}\right) \right] \\ & \times \exp\left(-\frac{k_l^2 w_1^2 w_2^2}{4(w_1^2 + w_2^2)}\right) \sqrt{\frac{N_{3-j}}{N_j}} (-1)^{j-3} \frac{\partial L_\Omega}{\partial x_{0j}} - \frac{\dot{N}_j}{N_j} \beta_j \end{aligned} \quad (\text{A2e})$$

Finally, the Euler equation of motion with respect to w_j is given by

$$\begin{aligned} \frac{N_j}{2w_j^3} + \frac{N_j^2}{2\sqrt{2\pi}w_j^2} \left[\epsilon_0 - \epsilon \sum_{l=1}^2 V_l (k_l^2 w_j^2 + 4) \exp\left(-\frac{k_l^2 w_j^2}{8}\right) \cos(k_l x_{0j}) \right] - \frac{N_j w_j}{2} \sum_{l=1}^2 (V_l k_l^2) \cos(k_l x_{0j}) \exp\left(-\frac{k_l^2 w_j^2}{4}\right) \\ + \frac{N_1 N_2 \eta_0 w_j}{\sqrt{\pi}(w_1^2 + w_2^2)^{5/2}} (w_1^2 + w_2^2 - 2(x_{01} - x_{02})^2) \exp\left(-\frac{(x_{01} - x_{02})^2}{w_1^2 + w_2^2}\right) \\ - \frac{\eta N_1 N_2 w_j}{2\sqrt{\pi}(w_1^2 + w_2^2)^{5/2}} \exp\left(-\frac{(x_{01} - x_{02})^2}{w_1^2 + w_2^2}\right) \sum_{l=1}^2 V_l \left[(-4(x_{01} - x_{02})^2 + 2w_1^2 + 2w_2^2 + k_l^2 \omega_{3-j}^4) \cos\left(k_l \frac{w_1^2 x_{02} + w_2^2 x_{01}}{w_1^2 + w_2^2}\right) \right. \\ \left. + (-1)^j 4k_l (x_{01} - x_{02}) \omega_{3-j}^2 \sin\left(k_l \frac{w_1^2 x_{02} + w_2^2 x_{01}}{w_1^2 + w_2^2}\right) \right] \exp\left(-\frac{k_l^2 w_1^2 w_2^2}{4(w_1^2 + w_2^2)}\right) - \sqrt{N_j N_{3-j}} \frac{\partial L_\Omega}{\partial w_j} = 0 \end{aligned} \quad (\text{A2f})$$

Note that the equation of motion corresponding to w_j does not contain the time derivative of the condensate width w_j as like the other equations (A2b)-(A2e). Due to this reason, the variational approach does not seem to fit to analyze the dynamics of the width of the condensate. The detailed equation for the effective potential V_j^{eff} can be derived

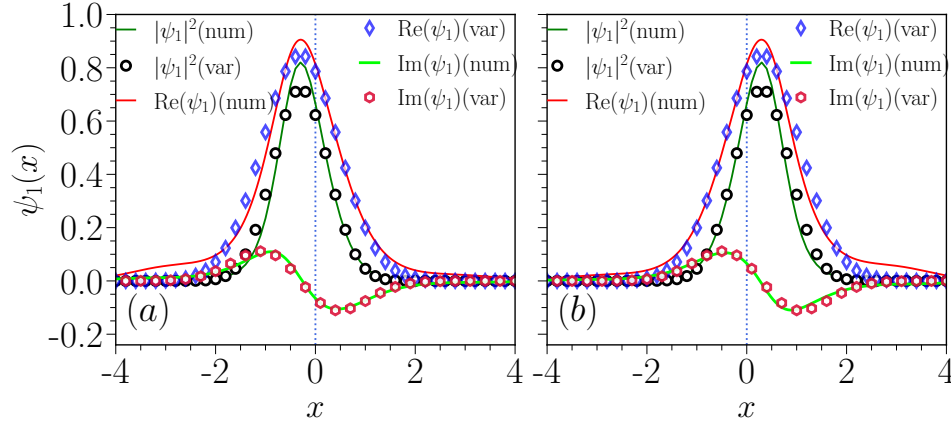


FIG. A.1. Comparison of the condensate density profile obtained numerically (solid line) and using the variational approach (open markers) for different inhomogeneity parameters when the phase difference between the nonlinear inhomogeneity and potential is $\pi/2$. (a) For $\epsilon = -\eta = -0.8$, and (b) For $\epsilon = -\eta = 0.8$. The other parameters are $k_L = 0.6$, $\theta_l = \pi/2k_l$, and $\Omega = 1.0$. Incorporating the phase shift $\pi/2$ between the potential and inhomogeneity results in the condensate localizing at an off-center position at (a) $x = -0.3$ and (b) $x = 0.3$. The real (Re) and imaginary (Im) parts of the condensate wavefunction show good agreement between the wave function profile obtained from numerical simulation and that from using the variational approach.

from the Eq. (A2c) and Eq. (A2e) and it will assume the form as

$$\begin{aligned}
V_j^{\text{eff}} = & -\frac{\epsilon}{2^{3/2}\sqrt{\pi}w_j} \sum_{l=1}^2 V_l \cos(k_l x_{0j}) \exp\left(-\frac{k_l^2 w_j^2}{8}\right) - \sum_{l=1}^2 V_l \cos(k_l x_{0j}) \exp\left(-\frac{k_l^2 w_j^2}{4}\right) + \frac{(-1)^{3-j}\eta_0}{\sqrt{\pi}(w_1^2 + w_2^2)^{1/2}} \\
& \times \exp\left(-\frac{(x_{01} - x_{02})^2}{w_1^2 + w_2^2}\right) - \frac{\eta}{\sqrt{\pi}\sqrt{w_1^2 + w_2^2}} \exp\left(-\frac{(x_{01} - x_{02})^2}{w_1^2 + w_2^2}\right) \sum_{l=1}^2 V_l \cos\left(\frac{k_l(w_1^2 x_{02} + w_2^2 x_{01})}{w_1^2 + w_2^2}\right) \\
& \times \exp\left(-\frac{k_l^2 w_1^2 w_2^2}{4(w_1^2 + w_2^2)}\right) + L_\Omega
\end{aligned} \tag{A3a}$$

The effective potential obtained in Eq. (A3a) is mainly composed of five different terms. The first term involving interactions ϵ contributes towards localization in case of repulsive interactions. The second term, containing the bichromatic optical lattice potential, is responsible for the localization of the condensate. The third term contains η_0 , which determines the state of localization or delocalization depending upon the component and the sign of η_0 . The last term containing the Rabi-coupling [See Eq. (A3a)] contributes towards either localization or delocalization for in-phase or out-of-phase state of the condensate, respectively. For our calculation, we choose $\phi = \pi$ between two components in all cases which implies that the role of Rabi coupling towards localization. Further, the condensate width w , and chirp β appearing in the effective potential can be estimated by solving Eqs. (10a–10c). After substituting the w_j , and β_j , we compute the $V^{\text{eff}}(x_0)$ for various spatial inhomogeneity and coupling parameters, which has been depicted in Fig. 12.

Appendix B: Details of the Lagrangian and effective potential for the phase shift $\pi/2$ between optical lattice potential and nonlinearity

In this appendix section, we provide the Lagrangian and the corresponding equation of the effective potential for the case of $\theta = \pi/2$ between optical lattice and interaction inhomogeneity. Here, $j = 1, 2$ represents the spin-up and spin-down components, respectively.

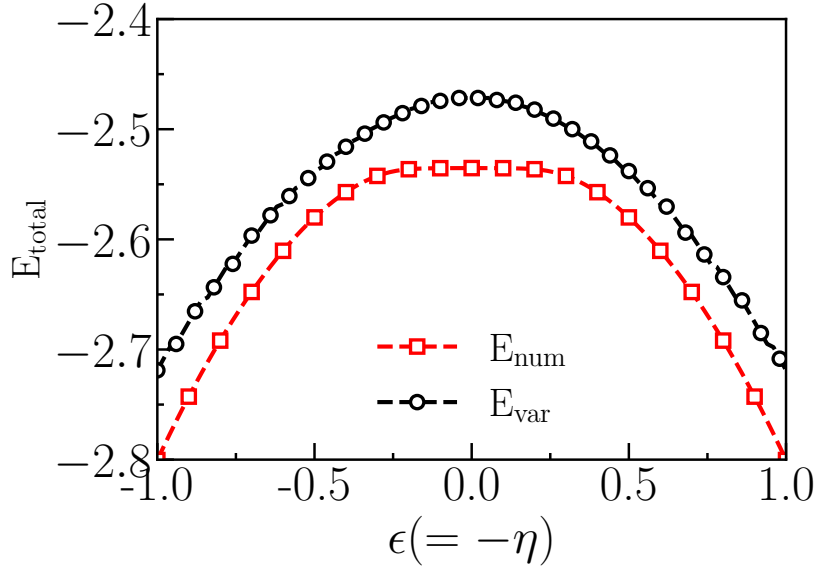


FIG. B.1. Variation of numerical (E_{num}) and variational (E_{var}) total energy with inhomogeneity $\epsilon(= -\eta)$ with $k_L = 0.6$, and $\Omega = 1.0$. Tuning the inhomogeneity leads to a monotonic decrease in the total energy in the localized regions, that is $-1 \lesssim \epsilon(= -\eta) \lesssim -0.3$ or $0.3 \lesssim \epsilon(= -\eta) \lesssim 1.0$ whereas, in the delocalized region $-0.3 \lesssim |\epsilon(= -\eta)| \lesssim 0.3$, the total energy remains almost constant at $E_{\text{num}} \sim -2.56$. In both cases, energy follow a symmetric nature in either side of delocalization regions.

$$\begin{aligned}
L = & \sum_{j=1}^2 \left[N_j (-1)^j \beta_j \dot{x}_{0_j} - N_j \dot{\phi}_j + N_j \beta_j k_L - \frac{N_j}{2} \left(\frac{1}{2w_j^2} + \beta_j^2 \right) - \frac{N_j}{2^{3/2} \sqrt{\pi} w_j} \left[\epsilon_0 - \epsilon \sum_{l=1}^2 V_l \sin(k_l x_{0_j}) \exp\left(-\frac{k_l^2 w_j^2}{8}\right) \right] \right. \\
& \left. + N_j \sum_{l=1}^2 V_l \cos(k_l x_{0_j}) \exp\left(-\frac{k_l^2 w_j^2}{4}\right) \right] - \frac{N_1 N_2}{\sqrt{\pi} \sqrt{w_1^2 + w_2^2}} \exp\left(-\frac{(x_{01} - x_{02})^2}{w_1^2 + w_2^2}\right) \\
& \times \left[\eta_0 + \eta \sum_{l=1}^2 V_l \sin\left(\frac{k_l (w_1^2 x_{02} + w_2^2 x_{01})}{w_1^2 + w_2^2}\right) \exp\left(-\frac{k_l^2 w_1^2 w_2^2}{4(w_1^2 + w_2^2)}\right) \right] - 2\sqrt{N_1 N_2} L_\Omega
\end{aligned} \tag{B1a}$$

In the above equation L_Ω has the same form as in Eq. (A1b). The effective potential V_{eff} assumes the form as,

$$\begin{aligned}
V_j^{\text{eff}} = & -\frac{\epsilon}{2^{3/2} \sqrt{\pi} w_j} \sum_{l=1}^2 V_l \sin(k_l x_{0_j}) \exp\left(-\frac{k_l^2 w_j^2}{8}\right) - \sum_{l=1}^2 V_l \cos(k_l x_{0_j}) \exp\left(-\frac{k_l^2 w_j^2}{4}\right) - \frac{\eta_0}{\sqrt{\pi} (w_1^2 + w_2^2)^{1/2}} \\
& \times \exp\left(-\frac{(x_{01} - x_{02})^2}{w_1^2 + w_2^2}\right) + \frac{\eta}{\sqrt{\pi} \sqrt{w_1^2 + w_2^2}} \exp\left(-\frac{(x_{01} - x_{02})^2}{w_1^2 + w_2^2}\right) \sum_{l=1}^2 V_l \sin\left(\frac{k_l (w_1^2 x_{02} + w_2^2 x_{01})}{w_1^2 + w_2^2}\right) \\
& \times \exp\left(-\frac{k_l^2 w_1^2 w_2^2}{4(w_1^2 + w_2^2)}\right) + L_\Omega
\end{aligned} \tag{B1b}$$

In Fig. A.1(a) and Fig. A.1(b), we show a comparison between the density profiles obtained from the numerical simulation (solid lines) and that from the variational approach (marked with open markers) for $\epsilon = -0.8$, $\eta = 0.8$ and $\epsilon = 0.8$, $\eta = -0.8$, respectively. For both the combination of the strength of the inhomogeneity, the condensate gets localized at off-center. For instance, in Fig. A.1(a), the condensate gets localized at $x \approx -0.3$, while, in Fig. A.1(b), the localization happens at $x \approx 0.3$. To unravel the reason for this particular nature of localization of the condensate at the off-center position in space, we analyze the nature of effective potential as depicted in Fig. 13(a). We find that increasing the strength of interaction results in shifting the minima of the effective potential V^{eff} either left or right, which depends solely on the nature of the interaction inhomogeneity. The left shift happens for the attractive ($\epsilon = -\eta = -1.0$) while the right shift happens for the repulsive intraspecies ($\epsilon = -\eta = 1.0$) interactions.

To get more insight into the probable cause for the localization and delocalization transition, in Fig. B.1, we show a variation of the total energy as a function of the interaction inhomogeneity obtained from the numerical simulation and using the variational approach. The energy shows a monotonically decreasing trend with the interaction inhomogeneity strength for $0.3 \lesssim |\epsilon(= -\eta)| \lesssim 1$. However, for $0 \lesssim |\epsilon(= -\eta)| \lesssim 0.3$ the energy assumes the constant value around $E_{\text{num}} \approx -2.56$. Variational energy E_{var} qualitatively follows a similar trend as that of E_{num} in both localized and delocalized regions.

-
- [1] P. W. Anderson, Absence of diffusion in certain random lattices, *Phys. Rev.* **109**, 1492 (1958).
- [2] M. Cutler and N. F. Mott, Observation of anderson localization in an electron gas, *Phys. Rev.* **181**, 1336 (1969).
- [3] E. Abrahams, P. W. Anderson, D. C. Licciardello, and T. V. Ramakrishnan, Scaling theory of localization: Absence of quantum diffusion in two dimensions, *Phys. Rev. Lett.* **42**, 673 (1979).
- [4] P. A. Lee and T. V. Ramakrishnan, Disordered electronic systems, *Rev. Mod. Phys.* **57**, 287 (1985).
- [5] F. Evers and A. D. Mirlin, Anderson transitions, *Rev. Mod. Phys.* **80**, 1355 (2008).
- [6] D. S. Wiersma, P. Bartolini, A. Lagendijk, and R. Righini, Localization of light in a disordered medium, *Nature* **390**, 671 (1997).
- [7] F. Scheffold, R. Lenke, R. Tweer, and G. Maret, Localization or classical diffusion of light?, *Nature* **398**, 206 (1999).
- [8] T. Schwartz, G. Bartal, S. Fishman, and M. Segev, Transport and Anderson localization in disordered two-dimensional photonic lattices, *Nature* **446**, 52 (2007).
- [9] C. M. Aegerter, M. Störzer, S. Fiebig, W. Bührer, and G. Maret, Observation of Anderson localization of light in three dimensions, *J. Opt. Soc. Am. A* **24**, A23 (2007).
- [10] J. Topolancik, B. Ilic, and F. Vollmer, Experimental observation of strong photon localization in disordered photonic crystal waveguides, *Phys. Rev. Lett.* **99**, 253901 (2007).
- [11] R. Dalichaouch, J. P. Armstrong, S. Schultz, P. M. Platzman, and S. L. McCall, Microwave localization by two-dimensional random scattering, *Nature* **354**, 53 (1991).
- [12] C. Dembowski, H.-D. Gräf, R. Hofferbert, H. Rehfeld, A. Richter, and T. Weiland, Anderson localization in a string of microwave cavities, *Phys. Rev. E* **60**, 3942 (1999).
- [13] A. A. Chabanov, M. Stoytchev, and A. Z. Genack, Statistical signatures of photon localization, *Nature* **404**, 850 (2000).
- [14] P. Pradhan and S. Sridhar, Correlations due to localization in quantum eigenfunctions of disordered microwave cavities, *Phys. Rev. Lett.* **85**, 2360 (2000).
- [15] R. L. Weaver, Anderson localization of ultrasound, *Wave Motion* **12**, 129 (1990).
- [16] A. Lagendijk, B. v. Tiggelen, and D. S. Wiersma, Fifty years of Anderson localization, *Phys. Today* **62**, 24 (2009).
- [17] A. Aspect and M. Inguscio, Anderson localization of ultracold atoms, *Phys. Today* **62**, 30 (2009).
- [18] J. Billy, V. Josse, Z. Zuo, A. Bernard, B. Hambrecht, P. Lugan, D. Clément, L. Sanchez-Palencia, P. Bouyer, and A. Aspect, Direct observation of Anderson localization of matter waves in a controlled disorder, *Nature* **453**, 891 (2008).
- [19] G. Roati, C. D’Errico, L. Fallani, M. Fattori, C. Fort, M. Zaccanti, G. Modugno, M. Modugno, and M. Inguscio, Anderson localization of a non-interacting Bose-Einstein condensate, *Nature* **453**, 895 (2008).
- [20] D. S. Hall, M. R. Matthews, J. R. Ensher, C. E. Wieman, and E. A. Cornell, Dynamics of component separation in a binary mixture of Bose-Einstein condensates, *Phys. Rev. Lett.* **81**, 1539 (1998).
- [21] E. A. Ostrovskaya and Y. S. Kivshar, Localization of two-component Bose-Einstein condensates in optical lattices, *Phys. Rev. Lett.* **92**, 180405 (2004).
- [22] K.-T. Xi, J. Li, and D.-N. Shi, Localization of a two-component Bose-Einstein condensate in a two-dimensional bichromatic optical lattice, *Phys. B: Condens.* **436**, 149 (2014).
- [23] Y.-J. Lin, K. Jiménez-García, and I. B. Spielman, Spin-orbit-coupled Bose-Einstein condensates, *Nature* **471**, 83 (2011).
- [24] Y. Cheng, G. Tang, and S. K. Adhikari, Localization of a spin-orbit-coupled Bose-Einstein condensate in a bichromatic optical lattice, *Phys. Rev. A* **89**, 063602 (2014).
- [25] C. Li, F. Ye, Y. V. Kartashov, V. V. Konotop, and X. Chen, Localization-delocalization transition in spin-orbit-coupled Bose-Einstein condensate, *Sci. Rep.* **6**, 31700 (2016).
- [26] W.-Y. Wang, F.-Q. Dou, and W.-S. Duan, Interaction induced localization of a spin-orbit-coupled Bose-Einstein condensate in a double-well potential, *Eur. Phys. J. D* **73**, 1 (2019).
- [27] M. C. P. dos Santos and W. B. Cardoso, Anderson localization induced by interaction in linearly coupled binary Bose-Einstein condensates, *Phys. Rev. E* **103**, 052210 (2021).
- [28] D. A. Zezyulin and V. V. Konotop, Localization of ultracold atoms in Zeeman lattices with incommensurate spin-orbit coupling, *Phys. Rev. A* **105**, 063323 (2022).
- [29] Z. Oztas, Spin orbit coupled Bose-Einstein condensate in a two dimensional bichromatic optical lattice, *Phys. Lett. A* **383**, 504 (2019).
- [30] L. Sanchez-Palencia, D. Clément, P. Lugan, P. Bouyer, G. V. Shlyapnikov, and A. Aspect, Anderson localization of expanding Bose-Einstein condensates in random potentials, *Phys. Rev. Lett.* **98**, 210401 (2007).
- [31] S. K. Adhikari and L. Salasnich, Localization of a Bose-Einstein condensate in a bichromatic optical lattice, *Phys. Rev. A* **80**, 023606 (2009).
- [32] S. K. Adhikari, Localization of a Bose-Einstein condensate vortex in a bichromatic optical lattice, *Phys. Rev. A* **81**, 043636 (2010).
- [33] Y. Cheng and S. K. Adhikari, Matter-wave localization in a random potential, *Phys. Rev. A* **82**, 013631 (2010).
- [34] Y. Cheng and S. K. Adhikari, Symmetry breaking in a localized interacting binary Bose-Einstein condensate in

- a bichromatic optical lattice, *Phys. Rev. A* **81**, 023620 (2010).
- [35] Y. Cheng and S. K. Adhikari, Localization of collisionally inhomogeneous condensates in a bichromatic optical lattice, *Phys. Rev. A* **83**, 023620 (2011).
- [36] Y. Cheng and S. K. Adhikari, Spatially-antisymmetric localization of matter wave in a bichromatic optical lattice, *Laser Phys. Lett.* **7**, 824 (2010).
- [37] P. O. Fedichev, Y. Kagan, G. V. Shlyapnikov, and J. T. M. Walraven, Influence of nearly resonant light on the scattering length in low-temperature atomic gases, *Phys. Rev. Lett.* **77**, 2913 (1996).
- [38] M. Theis, G. Thalhammer, K. Winkler, M. Hellwig, G. Ruff, R. Grimm, and J. H. Denschlag, Tuning the scattering length with an optically induced Feshbach resonance, *Phys. Rev. Lett.* **93**, 123001 (2004).
- [39] G. Theocharis, P. Schmelcher, P. G. Kevrekidis, and D. J. Frantzeskakis, Matter-wave solitons of collisionally inhomogeneous condensates, *Phys. Rev. A* **72**, 033614 (2005).
- [40] M. I. Rodas-Verde, H. Michinel, and V. M. Pérez-García, Controllable soliton emission from a Bose-Einstein condensate, *Phys. Rev. Lett.* **95**, 153903 (2005).
- [41] A. V. Carpentier, H. Michinel, M. I. Rodas-Verde, and V. M. Pérez-García, Analysis of an atom laser based on the spatial control of the scattering length, *Phys. Rev. A* **74**, 013619 (2006).
- [42] G. Theocharis, P. Schmelcher, P. G. Kevrekidis, and D. J. Frantzeskakis, Dynamical trapping and transmission of matter-wave solitons in a collisionally inhomogeneous environment, *Phys. Rev. A* **74**, 053614 (2006).
- [43] J. Garnier and F. K. Abdullaev, Transmission of matter-wave solitons through nonlinear traps and barriers, *Phys. Rev. A* **74**, 013604 (2006).
- [44] P. Niarchou, G. Theocharis, P. G. Kevrekidis, P. Schmelcher, and D. J. Frantzeskakis, Soliton oscillations in collisionally inhomogeneous attractive Bose-Einstein condensates, *Phys. Rev. A* **76**, 023615 (2007).
- [45] J. Belmonte-Beitia, V. M. Pérez-García, V. Vekslerchik, and V. V. Konotop, Localized nonlinear waves in systems with time- and space-modulated nonlinearities, *Phys. Rev. Lett.* **100**, 164102 (2008).
- [46] S. Golam Ali and B. Talukdar, Coupled matter-wave solitons in optical lattices, *Ann. Phys.* **324**, 1194 (2009).
- [47] J. B. Sudharsan, R. Radha, and P. Muruganandam, Collisionally inhomogeneous Bose-Einstein condensates with binary and three-body interactions in a bichromatic optical lattice, *J. Phys. B* **46**, 155302 (2013).
- [48] Y. Cheng, Effective potential of two coupled binary matter wave bright solitons with spatially modulated nonlinearity, *J. Phys. B* **42**, 205005 (2009).
- [49] S. Roy, T. Mishra, B. Tanatar, and S. Basu, Reentrant localization transition in a quasiperiodic chain, *Phys. Rev. Lett.* **126**, 106803 (2021).
- [50] A. Padhan, M. K. Giri, S. Mondal, and T. Mishra, Emergence of multiple localization transitions in a one-dimensional quasiperiodic lattice, *Phys. Rev. B* **105**, L220201 (2022).
- [51] S. Roy, S. Chattopadhyay, T. Mishra, and S. Basu, Critical analysis of the reentrant localization transition in a one-dimensional dimerized quasiperiodic lattice, *Phys. Rev. B* **105**, 214203 (2022).
- [52] S. Roy and S. Basu, Interplay of off-diagonal random disorder and quasiperiodic potential in a one-dimensional Aubry-André model, *Europhys. Lett.* **128**, 47005 (2020).
- [53] C. Wu, J. Fan, G. Chen, and S. Jia, Non-hermiticity-induced reentrant localization in a quasiperiodic lattice, *New J. Phys.* **23**, 123048 (2021).
- [54] R. Qi, J. Cao, and X.-P. Jiang, Multiple localization transitions and novel quantum phases induced by a staggered on-site potential, *Phys. Rev. B* **107**, 224201 (2023).
- [55] X.-P. Jiang, Y. Qiao, and J.-P. Cao, Mobility edges and reentrant localization in one-dimensional dimerized non-Hermitian quasiperiodic lattice, *Chinese Phys. B* **30**, 097202 (2021).
- [56] S. Vaidya, C. Jörg, K. Linn, M. Goh, and M. C. Rechtsman, Reentrant delocalization transition in one-dimensional photonic quasicrystals, *Phys. Rev. Res.* **5**, 033170 (2023).
- [57] Z.-S. Xu, J. Gao, A. Iovan, I. M. Khaymovich, V. Zwiller, and A. W. Elshaari, Observation of reentrant metal-insulator transition in a random-dimer disordered ssh lattice (2023), [arXiv:2307.05207 \[cond-mat.dis-nn\]](https://arxiv.org/abs/2307.05207).
- [58] H. Sakaguchi and B. A. Malomed, Matter-wave solitons in nonlinear optical lattices, *Phys. Rev. E* **72**, 046610 (2005).
- [59] F. Abdullaev, A. Abdumalikov, and R. Galimzyanov, Gap solitons in Bose-Einstein condensates in linear and nonlinear optical lattices, *Phys. Lett. A* **367**, 149 (2007).
- [60] J. L. Bohn and P. S. Julienne, Prospects for influencing scattering lengths with far-off-resonant light, *Phys. Rev. A* **56**, 1486 (1997).
- [61] R. Ciuryło, E. Tiesinga, and P. S. Julienne, Optical tuning of the scattering length of cold alkaline-earth-metal atoms, *Phys. Rev. A* **71**, 030701 (2005).
- [62] R. Ciuryło, E. Tiesinga, and P. S. Julienne, Stationary phase approximation for the strength of optical Feshbach resonances, *Phys. Rev. A* **74**, 022710 (2006).
- [63] P. Muruganandam and S. K. Adhikari, Fortran programs for the time-dependent Gross-Pitaevskii equation in a fully anisotropic trap, *Comput. Phys. Commun.* **180**, 1888 (2009).
- [64] L. E. Young-S, D. Vudragović, P. Muruganandam, S. K. Adhikari, and A. Balaž, OpenMP Fortran and c programs for solving the time-dependent Gross-Pitaevskii equation in an anisotropic trap, *Comput. Phys. Commun.* **204**, 209 (2016).
- [65] R. Ravisankar, D. Vudragović, P. Muruganandam, A. Balaž, and S. K. Adhikari, Spin-1 spin-orbit- and Rabi-coupled Bose-Einstein condensate solver, *Comput. Phys. Commun.* **259**, 107657 (2021).
- [66] S. K. Sarkar, T. Mishra, P. Muruganandam, and P. K. Mishra, Quench-induced chaotic dynamics of Anderson-localized interacting Bose-Einstein condensates in one dimension, *Phys. Rev. A* **107**, 053320 (2023).
- [67] R. Ravisankar, T. Sriraman, L. Salasnich, and P. Muruganandam, Quenching dynamics of the bright solitons and other localized states in spin-orbit coupled Bose-Einstein condensates, *J. Phys. B* **53**, 195301 (2020).
- [68] R. Ravisankar, H. Fabreli, A. Gammal, P. Muruganandam, and P. K. Mishra, Effect of Rashba spin-orbit and Rabi couplings on the excitation spectrum of binary Bose-Einstein condensates, *Phys. Rev. A* **104**, 053315 (2021).
- [69] S. Gangwar, R. Ravisankar, S. I. Mistakidis, P. Muruganandam, and P. K. Mishra, Spectrum and quench-induced dynamics of spin-orbit-coupled quantum droplets, *Phys. Rev. A* **109**, 013321 (2024).